8-2011

On the Bidirectional Vortex Engine Flowfield with Arbitrary Endwall Injection

Georges Akiki
gakiki@utk.edu

To the Graduate Council:

I am submitting herewith a thesis written by Georges Akiki entitled "On the Bidirectional Vortex Engine Flowfield with Arbitrary Endwall Injection." I have examined the final electronic copy of this thesis for form and content and recommend that it be accepted in partial fulfillment of the requirements for the degree of Master of Science, with a major in Aerospace Engineering.

Joseph Majdalani, Major Professor

We have read this thesis and recommend its acceptance:

Trevor M. Moeller, Christian G. Parigger

Accepted for the Council:
Carolyn R. Hodges

Vice Provost and Dean of the Graduate School

(Original signatures are on file with official student records.)

On the Bidirectional Vortex Engine Flowfield with Arbitrary Endwall Injection

A Thesis Presented for

the Master of Science

Degree

The University of Tennessee, Knoxville

Georges Henri Akiki

August 2011

Dedication

This thesis is dedicated to my beloved parents, Henri and Hoda, and my brothers Michel and Lucien. Their unbounded faith and support paved the way to pursue my dreams. For their love I owe all the blessings in my life.

Acknowledgments

I would like to thank Dr. Majdalani who guided me with his advice and mentorship throughout the research that led to this thesis. I would also like to thank my committee members, Dr. Moeller and Dr. Parigger, for taking the time to help ameliorate this work.

I would like to thank my brother and teammate Michel Akiki who provided great support towards completing this study.

Abstract

In an attempt to generalize previous models of the bidirectional vortex mean flow, a new solution is presented that can cope with arbitrary injections and outlet conditions. In the process, the steady, inviscid and axisymmetric equations of motions are reduced to one partial differential equation for the stream function, known as the Bragg-Hawthorne equation, which is solved exactly. The solution is shown to be highly dependent on the imposed boundary conditions: the mean flow changes according to the manner by which the fluid is injected or extracted from the vortex chamber. From the stream function, the velocity is obtained along with the vorticity and pressure distributions which are carefully derived and analyzed. The results are then compared to several inviscid models found in the literature. After determining an exact inviscid solution to the problem, viscous effects at the core are added to overcome the known singularity that arises at the centerline. The governing equations are hence revisited while keeping the viscous diffusion term in the tangential momentum equation. The core region, where viscous effects lead to the onset of a forced vortex, is rescaled using appropriate transformations. An asymptotic approximation is then applied to linearize and solve the resulting ODE for the tangential

velocity. The inner viscous solution is then matched to the outer inviscid result using Prandtl's Matching Principle. Finally, the viscous correction is passed onto the vorticity and pressure formulations.

Table of Contents

List of Figures

Nomenclature

A_i = inlet area

a = chamber radius

B = tangential angular momentum, ru_θ

b = chamber outlet radius

C = swirl momentum constant

D = tangential surface parameter

H = stagnation pressure head

L = chamber length

l = chamber aspect ratio, L / a

p = pressure

Q_i = inlet volumetric flow rate

Re = injection Reynolds number, $\rho Ua / \mu$

r, θ, z = radial, tangential, and axial coordinates

U = mean tangential (inflow) velocity

$U_0(r)$ = arbitrary axial velocity at the headwall

$U_L(r)$ = arbitrary axial velocity at the endwall

u_r = dimensional radial velocity

u_θ = dimensional tangential velocity

u_z = dimensional axial velocity

$\boldsymbol{u}$ = velocity vector

Symbols

κ = tangential inflow parameter, $(2\pi\sigma l)^{-1}$

λ_n = nth zero of J_1, the Bessel function of the first kind

σ = swirl number, a^2 / A_i

υ = separation constant

ψ = stream function

$\bar{}$ = overbars denote a non-dimensional variable

ω = vorticity

ω_f = angular velocity

ρ = density

ε = perturbation parameter, $1 / \mathrm{Re}$

Subscripts

r, θ, z = radial, tangential and axial components

Superscripts

(o) = outer (inviscid) solution

(i) = inner (viscous) solution

(c) = composite solution

(cl) = common limit

Chapter 1

Introduction

Since the discovery of the rockets in the 13th century, researchers have been seeking to improve their efficiency, reliability and applicability in propulsion and payload delivery. Today, rockets are the sole means of transportation between Earth and outer space.

Rockets using chemical propulsion can generally be classified into three categories: solid, liquid and hybrid propellant rockets [1]. Solid rockets motors (SRMs) use premixed fuel and oxidizer to form the propellant that is mounted along the sidewalls of a combustion chamber. Although it is the simplest of the 3 categories, SRMs do not provide the possibility of throttling the thrust, which is an important feature for precise maneuvers. Liquid rockets on the other hand consist of liquid fuel and oxidizer stored in separate tanks (i.e., in the case of a bipropellant). When pumped into the combustion chamber, chemical reactions take place from which thrust is generated. Although it is more complicated and expensive to build, liquid rockets offer the user control over the

quantity of fuel being pumped into the chamber, therefore, adjusting the thrust. Hybrids were introduced as a combination of the two previous types [2, 3]. Their propellant consists of solid fuel grains mounted on the sidewalls, and the liquid oxidizer which is stored in a tank before being injected into the chamber. This setup takes advantage of the simplicity of SRMs and the controllability of liquid rocket engines.

A subset of the liquid and hybrid category is known as the "vortex engine" [4]. This particular configuration makes use of cyclonic motion to create a bidirectional vortex inside a combustion chamber.

1.1 Cyclonic Motion

Besides their emergence in naturally occurring phenomena, cyclonic motions arise in a variety of industrial and propulsion related applications. These swirl-induced patterns are connected to meteorological events such as tornadoes, hurricanes and typhoons [5], as well as astronomical activities such as cosmic spirals and galactic pinwheels [6, 7]. The bidirectional type of motion is also employed in industrial processes involving cyclonic separators, combustors, and furnaces [8]. The main interest here is tied to the cyclonic motion that is engendered in the vortex-fired engine class of propulsion devices. This class encompasses several innovative internal combustion devices and thrust chambers such as the (unidirectional) Vortex Hybrid Engine introduced by Gloyer, Knuth and Goodman [9], the Vortex Injection Hybrid Rocket Engine conceived by Knuth *et al*. [10], the Vortex Combustion Cold-Wall Chamber

developed by Chiaverini *et al.* [11], and the Reverse Vortex Combustor invented by Matveev *et al*. [12]. Several of these studies are described in a paper by Majdalani [13].

Prior to the work conducted in rocket engines, studies have primarily focused on modeling cyclonic flows. One of the earliest studies was the work by Rankine [14] in which he separated the swirl motion into a free and forced motion. Studies by Lamb [15] and Oseen [16] followed Rankine's and provided marked improvements in dimensionality and modeling capability. The Lamb-Oseen vortex decays with time mainly due to shear. Burgers [17, 18] and Rott [19, 20] also presented a vortex model that is spatial dependent, unlike the Lamb-Oseen vortex which is time-dependent.

Much fewer models that represent bidirectional vortex motion can be found in the literature. The first to present an exact solution for similar flowfields was perhaps Sullivan [21] with his two-cell vortex, and this was followed by Bloor and Ingham [22] whose work was extended by Barber and Majdalani [23]. An extensive historical survey of the advancements in modeling confined vortices is presented by Batterson, Maicke and Majdalani [24].

In parallel to the theoretical modeling of vortex-dominated flows, several experiments were conducted to better understand the behavior of swirling motions, such as the ones by Kelsall [25] and Smith [26, 27]. Some numerical investigations were also performed, including those by: Hoekstra, Derksen and van den Akker [28], Derksen and van den Akker [29], Fang, Majdalani and Chiaverini [30], and Rom, Anderson and Chiaverini [31].

1.2 Inviscid Models

Given the shortage of purely analytical models of axisymmetric cyclonic flows, an Eulerian-based solution was developped by Vyas and Majdalani [32] and also by Majdalani and Rienstra [33], using a right-cylindrical Vortex Combustion Cold-Wall Chamber model. Their model is known as the Complex-Lamellar profile. Shortly thereafter, an extension to the hybrid vortex configuration was conceived and carried out by Majdalani and Vyas [34], and later generalized by Majdalani [35] for the case involving sidewall mass addition. In a more recent study by Majdalani [13], a series of exact solutions are presented in the form of Beltramian and Trkalian helical motions. Additional models that extend to cover the hybrid class of engines are also offered in that study.

1.3 Viscous Models

Extensions to the inviscid models were introduced to take into account viscosity and the boundary layers generated both at the core and sidewall regions. Majdalani and Chiaverini [36] presented the core and sidewall corrections to the Complex-Lamellar model. These were resolved under laminar conditions for the tangential velocity and then for the axial and radial orientations by Batterson and Majdalani [37, 38]. A piecewise representation of the problem leading to a Rankine-like vortex was also developed by Maicke and Majdalani [39] in which the effect of a turbulent eddy viscosity is discussed.

1.4 Bidirectional Vortex

The innovative characteristic of the vortex engine is that the oxidizer is injected near the nozzle tangentially. The resulting swirling motion gives rise to an outer vortex over the entire length of the chamber. When it reaches the headwall, the flow reverses direction and forms an inner vortex traveling the chamber back again before exiting through the nozzle. The outer vortex consists of low temperature gases, thus creating a self-cooling mechanism for the chamber walls. This scenario offers the possibility for:

- Eliminating the need for leak-prone cooling passages.
- Extending the operational lifetimes of combustion chambers.
- Making combustion chamber walls using relatively inexpensive and easier to shape materials, possibly even lightweight composites, instead of expensive alloys.

1.5 Scope

The purpose of this study is to find a general solution for the mean cold flow in a vortex engine that can account for arbitrary inlet and outlet conditions. The problem definition is presented in Chapter 2, for which an inviscid solution is developed in Chapter 3. Results of the inviscid exact solution are discussed in Chapter 4 and then followed in Chapter 5 by a core viscous correction that is needed to overcome the singularity in the inviscid solution. The viscous corrected solution is described in more detail in Chapter 6, while conclusions and recommendations for future work are offered in Chapter 7.

Chapter 2

Problem Definition

2.1 Geometry

The geometry of a vortex engine can be idealized as a cylindrical chamber. The model is sketched in Figure 2-1, showing the chamber length L and radius a. In the cylindrical coordinate system, the variable z denotes the axial direction, r the radial direction, and θ the azimuthal component.

Note that an inlet section is located near $z = L$ (the endwall) to permit the injection of an oxidizer with arbitrary velocity. The fuel is injected at the headwall where $z = 0$. Both fluids will then transverse the length of the chamber in an inner vortex and exit at the outlet that has an inner radius b.

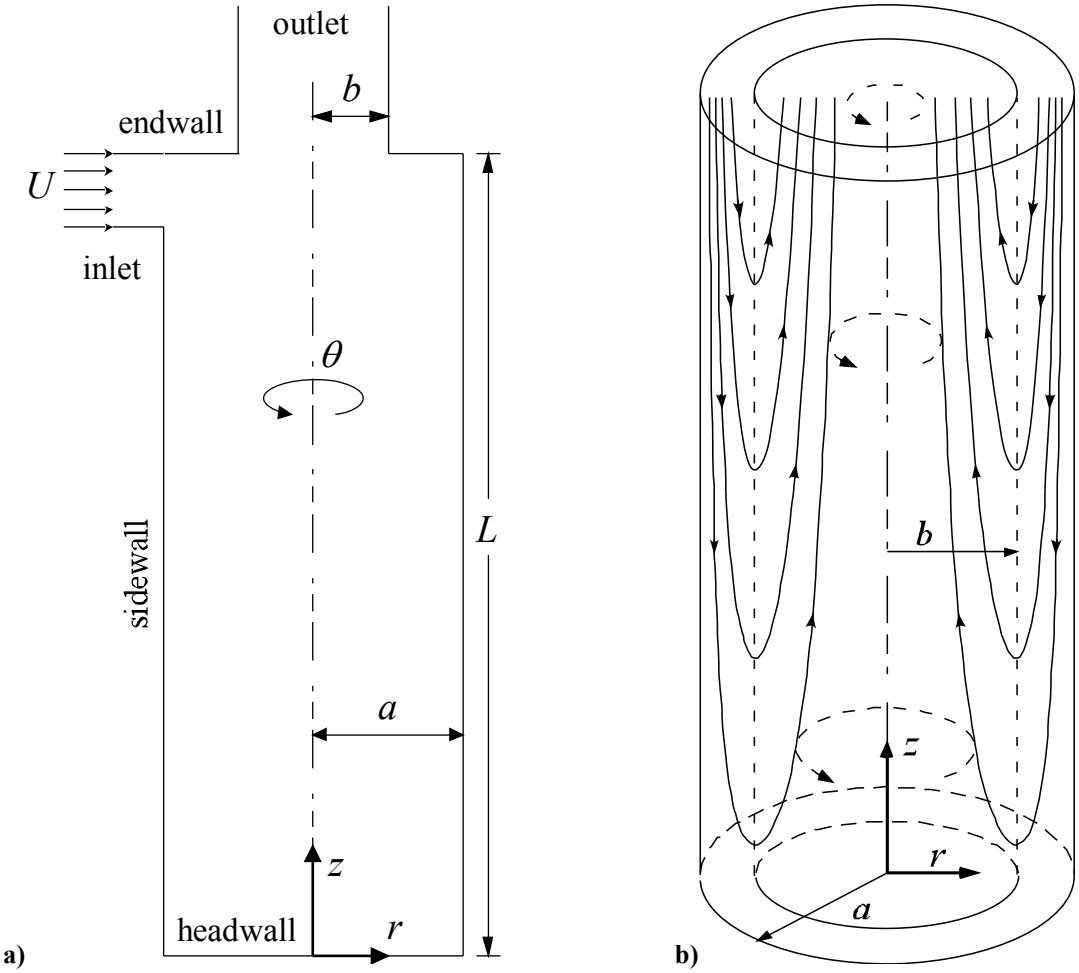

Figure 2-1. Schematic of the cylindrical bidirectional vortex chamber showing a) geometric and b) flowfield characteristics.

2.2 Governing Equations

The purpose of this work is to solve for the internal flowfield of a vortex engine using cylindrical geometry. The assumptions used to idealize and simplify the problem include steady-state conditions, inviscid flow, and incompressible fluid.

2.3 Conservation of Mass

For steady motions, the continuity equation reduces to

$$\nabla \cdot (\rho \boldsymbol{u}) = \vec{0} \tag{2.1}$$

The velocity vector u is composed of the axial, normal and tangential components denoted by u_r, u_θ and u_z respectively. Using the incompressibility ($\rho = \text{const}$) and axisymmetric (no θ–dependency) assumptions, Eq. (2.1) reduces to

$$\frac{1}{r}\frac{\partial (r u_r)}{\partial r} + \frac{\partial u_z}{\partial z} = 0 \tag{2.2}$$

2.4 Conservation of Momentum

The conservation of momentum equations may be reduced according to the assumptions listed above. Furthermore, the first part of this study will be concerned in developing an exact inviscid model; therefore, the viscous terms are ignored. The momentum equation condenses to

$$u_r \frac{\partial u_z}{\partial r} + u_z \frac{\partial u_z}{\partial z} = -\frac{1}{\rho}\frac{\partial p}{\partial z} \text{ (axial momentum)} \tag{2.3}$$

$$u_r \frac{\partial u_r}{\partial r} - \frac{u_\theta^2}{r} + u_z \frac{\partial u_r}{\partial z} = -\frac{1}{\rho}\frac{\partial p}{\partial r} \text{ (radial momentum)} \tag{2.4}$$

$$u_r \frac{\partial u_\theta}{\partial r} + \frac{u_\theta u_r}{r} + u_z \frac{\partial u_\theta}{\partial z} = 0 \text{ (tangential momentum)} \tag{2.5}$$

Note that the effects of gravity are insignificant compared to the magnitude of the fluid momentum involved in these types of flows.

2.5 Boundary Conditions

Understanding the physical requirements for this problem, one is able to define specific boundary conditions that lead to a meaningful representation of the mean flow.

To start, we assume that no fluid penetrates the sidewalls, as in the case of the liquid vortex engine. We also assume that the flow is axisymmetric, so the radial velocity at the centerline may be set equal to zero. Conversely, the axial velocities at the endwall and headwall are left arbitrary. This allows the solution to be general and gives it the ability to adjust the mean flow according to the changes in the injection mode. The solution must be able to match the injected tangential velocity at the endwall, which is also arbitrary. Finally, the reference pressure is taken at the corner of the headwall. Mathematically, these boundary conditions translate into:

$$u_r(a,z) = 0 \text{ (impermeable sidewall)} \tag{2.6}$$

$$u_r(0,z) = 0 \text{ (axisymmetric motion)} \tag{2.7}$$

$$u_z(r,L) = U_L(r) \text{ (arbitrary axial profile at endwall)} \tag{2.8}$$

$$u_z(r,0) = U_0(r) \text{ (arbitrary axial profile at headwall)} \tag{2.9}$$

$$u_\theta(r,L) = U_\theta(r) \text{ (arbitrary tangential profile at endwall)} \tag{2.10}$$

$$p(a,0) = P_0 \quad \text{(reference pressure)} \tag{2.11}$$

To be able to specify physical boundary conditions, one should be familiar with the method a vortex engine behaves. For example, $U_L(r)$ should be a profile that has positive value near the core (extraction of fluid) and negative close to the sidewalls (introduction of fluid). A possible profile in this case may be something of the form

$$U_L = \cos(r^2 / a) + c \tag{2.12}$$

The axial profiles should also insure that the same quantity of fluid injected to the chamber should also exit in order to be physically plausible.

Concerning the tangential boundary condition, a typical profile would have the same characteristics as a free vortex given by

$$U_\theta(r) = \frac{a}{r} \tag{2.13}$$

Now that the governing equations and boundary conditions have been fully defined, solutions will be presented in Chapter 3.

Chapter 3

Solution Formulation

3.1 Stream Function Transformation

Introducing the stream function ψ, such that $u_z = r^{-1}\partial\psi/\partial r$ and $u_r = -r^{-1}\partial\psi/\partial z$, the momentum equations, coupled with the continuity equation, may be transformed into a single expression known as the Bragg-Hawthorne equation (BHE),

$$\frac{\partial^2\psi}{\partial z^2} + \frac{\partial^2\psi}{\partial r^2} - \frac{1}{r}\frac{\partial\psi}{\partial r} = r^2\frac{\mathrm{d}H}{\mathrm{d}\psi} - B\frac{\mathrm{d}B}{\mathrm{d}\psi} \tag{3.1}$$

Here $H = p/\rho + \frac{1}{2}u^2$ and $B = ru_\theta$ represent the total pressure head and tangential angular momentum, respectively.

In the absence of friction and heat addition, isentropic conditions may be assumed. This enables us to set $\mathrm{d}H/\mathrm{d}\psi = 0$ as done previously, for example, by Bloor and Ingham [22].

To further simplify the problem, we follow the approach used by Majdalani [13] and take the second term on the right-hand-side (RHS) of Eq. (3.1) to be a linear function of ψ. Thus using C to define the dimensional, *swirl momentum constant*, we put

$$B\frac{\mathrm{d}B}{\mathrm{d}\psi} = C^2\psi \tag{3.2}$$

and collect

$$\frac{\partial^2\psi}{\partial z^2} + \frac{\partial^2\psi}{\partial r^2} - \frac{1}{r}\frac{\partial\psi}{\partial r} + C^2\psi = 0 \tag{3.3}$$

Equation (3.3) can then be solved using separation of variables.

3.2 Solution

Substituting $\psi(z,r) = Z(z)R(r)$ into Eq. (3.3) leads to

$$-\frac{1}{Z(z)}\frac{\mathrm{d}^2Z(z)}{\mathrm{d}z^2} = \frac{1}{R(r)}\frac{\mathrm{d}^2R(r)}{\mathrm{d}r^2} - \frac{1}{rR(r)}\frac{\mathrm{d}R(r)}{\mathrm{d}r} + C^2 = \begin{cases} 0 \\ \pm\upsilon^2 \end{cases} \tag{3.4}$$

Clearly, three cases may be identified and promptly classified, according to Majdalani [13], into

Type 0 with $\mathrm{RHS} = 0$:

$$\psi(r,z) = r\left(C_1 z + C_2\right)\left[C_3 J_1\left(Cr\right) + C_4 Y_1\left(Cr\right)\right] \tag{3.5}$$

Type I with $\mathrm{RHS} = +\upsilon^2$:

$$\psi(r,z) = r\left[C_1\sin\left(\upsilon\, z\right) + C_2\cos\left(\upsilon\, z\right)\right]\left[C_3 J_1\left(r\sqrt{C^2-\upsilon^2}\right) + C_4 Y_1\left(r\sqrt{C^2-\upsilon^2}\right)\right] \tag{3.6}$$

Type II with $\mathrm{RHS} = -\upsilon^2$:

$$\psi(r,z) = r\left[C_1 \sinh(\upsilon\, z) + C_2 \cosh(\upsilon\, z)\right]\left[C_3 J_1\left(r\sqrt{C^2+\upsilon^2}\right) + C_4 Y_1\left(r\sqrt{C^2+\upsilon^2}\right)\right] \quad (3.7)$$

When imposing the centerline condition defined by Eq. (2.7), it may be realized that $C_4 = 0$ will eliminate the singularity for $r \to 0$ in $Y_1(Cr)$, $Y_1[r(C^2-\upsilon^2)^{\frac{1}{2}}]$ and $Y_1[r(C^2+\upsilon^2)^{\frac{1}{2}}]$. The solution set reduces to

$$\psi(r,z) = \begin{cases} r(K_1 z + K_2) J_1(Cr) & \text{(type 0)} \\ r\left[K_1 \sin(\upsilon z) + K_2 \cos(\upsilon z)\right] J_1\left(r\sqrt{C^2-\upsilon^2}\right) & \text{(type I)} \\ r\left[K_1 \sinh(\upsilon z) + K_2 \cosh(\upsilon z)\right] J_1\left(r\sqrt{C^2+\upsilon^2}\right) & \text{(type II)} \end{cases} \quad (3.8)$$

where $K_1 = C_1 C_3$ and $K_2 = C_2 C_3$. At this point one may apply Eq. (2.6), the rigid wall requirement on the radial velocity, to extract two sets of eigenvalues:

$$J_1\left(a\sqrt{C^2-\upsilon^2}\right) = 0 \qquad \text{or} \qquad \upsilon = \upsilon_n = \sqrt{C^2 - \lambda_n^2 / a^2} \qquad \text{(type I)} \quad (3.9)$$

$$J_1\left(a\sqrt{C^2+\upsilon^2}\right) = 0 \qquad \text{or} \qquad \upsilon = \upsilon_n^* = \sqrt{\lambda_n^2 / a^2 - C^2} \qquad \text{(type II)} \quad (3.10)$$

where λ_n designates the set of roots connected with the Bessel function of the first kind ($\lambda_0 = 3.83171,\ \lambda_1 = 7.01559,\ \lambda_2 = 10.1735...$). In what follows, the multivalued nature of λ_n warrants the use of both expressions for υ_n and υ_n^*. In the type 0 formulation, the stream function remains independent of υ, a situation that leads to a special solution, in which C remains single-valued, as prescribed by Eq. (3.2). A more comprehensive framework may be achieved by summing over all λ_n and putting, for the type I and type II solutions,

$$\psi(r,z)=\begin{cases}\displaystyle\sum_{n=0}^{\infty} r\left[K_{1n}\sin\left(\upsilon_n z\right)+K_{2n}\cos\left(\upsilon_n z\right)\right]J_1\left(\lambda_n r/a\right) & \text{(type I)}\\ \displaystyle\sum_{n=0}^{\infty} r\left[K_{1n}\sinh\left(\upsilon_n^* z\right)+K_{2n}\cosh\left(\upsilon_n^* z\right)\right]J_1\left(\lambda_n r/a\right) & \text{(type II)}\end{cases} \tag{3.11}$$

and, for the corresponding axial velocity,

$$u_z=\begin{cases}\displaystyle\sum_{n=0}^{\infty}\left[K_{1n}\sin\left(\upsilon_n z\right)+K_{2n}\cos\left(\upsilon_n z\right)\right]\frac{\lambda_n}{a}J_0\left(\frac{\lambda_n}{a}r\right) & \text{(type I)}\\ \displaystyle\sum_{n=0}^{\infty}\left[K_{1n}\sinh\left(\upsilon_n^* z\right)+K_{2n}\cosh\left(\upsilon_n^* z\right)\right]\frac{\lambda_n}{a}J_0\left(\frac{\lambda_n}{a}r\right) & \text{(type II)}\end{cases} \tag{3.12}$$

At this juncture, arbitrary velocity profiles may be imposed at the endwall and headwall by specifying $u_z(r,L)=U_L(r)$ and $u_z(r,0)=U_0(r)$ as per Eqs. (2.8) and (2.9). Using the orthogonality function, we recall that

$$\int_0^a rJ_0\left(mr\right)J_0\left(nr\right)\mathrm{d}r=\begin{cases}0; & m\neq n\\ \frac{1}{2}a^2J_0^2\left(ma\right); & m=n\end{cases} \tag{3.13}$$

Multiplying both sides of Eq. (3.12) by $rJ_0(\lambda_m r/a)$ and integrating form 0 to a, we obtain, at $z=0$:

$$\int_0^a rU_0(r)J_0\left(\frac{\lambda_n}{a}r\right)\mathrm{d}r=\begin{cases}\dfrac{1}{2}K_{2n}\lambda_n aJ_0^2\left(\dfrac{\lambda_n}{a}r\right) & \text{(type I)}\\ \dfrac{1}{2}K_{2n}\lambda_n aJ_0^2\left(\dfrac{\lambda_n}{a}r\right) & \text{(type II)}\end{cases} \tag{3.14}$$

and, at $z=L$:

$$\int_0^a rU_L(r)J_0\left(\frac{\lambda_n}{a}r\right)\mathrm{d}r=\begin{cases}\dfrac{1}{2}\left[K_{1n}\sin\left(\upsilon_n L\right)+K_{2n}\cos\left(\upsilon_n L\right)\right]\lambda_n aJ_0^2\left(\dfrac{\lambda_n}{a}r\right) & \text{(type I)}\\ \dfrac{1}{2}\left[K_{1n}\sinh\left(\upsilon_n^* L\right)+K_{2n}\cosh\left(\upsilon_n^* L\right)\right]\lambda_n aJ_0^2\left(\dfrac{\lambda_n}{a}r\right) & \text{(type II)}\end{cases} \tag{3.15}$$

Equations (3.14) and (3.15) are then solved for the two constants K_{1n} and K_{2n}. We find:

$$K_{1n}=\begin{cases}\dfrac{I_L-\cos\left(\upsilon_n L\right)I_0}{\lambda_n a J_0^2\left(\lambda_n\right)\sin\left(\upsilon_n L\right)}\\ \dfrac{I_L-\cosh\left(\upsilon_n^* L\right)I_0}{\lambda_n a J_0^2\left(\lambda_n\right)\sinh\left(\upsilon_n^* L\right)}\end{cases}\quad\text{and}\quad K_{2n}=\begin{cases}\dfrac{I_0}{\lambda_n a J_0^2\left(\lambda_n\right)}\\ \dfrac{I_0}{\lambda_n a J_0^2\left(\lambda_n\right)}\end{cases}\tag{3.16}$$

In the above, the source terms may be determined from

$$I_0\equiv 2\int_0^a U_0(r)rJ_0\left(\lambda_n r/a\right)\mathrm{d}r\quad\text{and}\quad I_L\equiv 2\int_0^a U_L(r)rJ_0\left(\lambda_n r/a\right)\mathrm{d}r\tag{3.17}$$

Inserting these relations back into Eq. (3.11) and differentiating, general expressions for the axial and radial velocities may be returned. These are

$$u_z=\begin{cases}\displaystyle\sum_{n=0}^{\infty}\left[\frac{I_L-\cos\left(\upsilon_n L\right)I_0}{\lambda_n a J_0^2\left(\lambda_n\right)}\frac{\sin\left(\upsilon_n z\right)}{\sin\left(\upsilon_n L\right)}+\frac{I_0\cos\left(\upsilon_n z\right)}{\lambda_n a J_0^2\left(\lambda_n\right)}\right]\frac{\lambda_n}{a}J_0\left(\frac{\lambda_n}{a}r\right) & \text{(type I)}\\ \displaystyle\sum_{n=0}^{\infty}\left[\frac{I_L-\cosh\left(\upsilon_n^* L\right)I_0}{\lambda_n a J_0^2\left(\lambda_n\right)}\frac{\sinh\left(\upsilon_n^* z\right)}{\sinh\left(\upsilon_n^* L\right)}+\frac{I_0\cosh\left(\upsilon_n^* z\right)}{\lambda_n a J_0^2\left(\lambda_n\right)}\right]\frac{\lambda_n}{a}J_0\left(\frac{\lambda_n}{a}r\right) & \text{(type II)}\end{cases}\tag{3.18}$$

and

$$u_r=\begin{cases}-\displaystyle\sum_{n=0}^{\infty}\left[\frac{I_L-\cos\left(\upsilon_n L\right)I_0}{\lambda_n a J_0^2\left(\lambda_n\right)}\frac{\upsilon_n\cos\left(\upsilon_n z\right)}{\sin\left(\upsilon_n L\right)}-\frac{I_0\upsilon_n\sin\left(\upsilon_n z\right)}{\lambda_n a J_0^2\left(\lambda_n\right)}\right]J_1\left(\frac{\lambda_n}{a}r\right) & \text{(type I)}\\ -\displaystyle\sum_{n=0}^{\infty}\left[\frac{I_L-\cosh\left(\upsilon_n^* L\right)I_0}{\lambda_n a J_0^2\left(\lambda_n\right)}\frac{\upsilon_n^*\cosh\left(\upsilon_n^* z\right)}{\sinh\left(\upsilon_n^* L\right)}+\frac{I_0\upsilon_n^*\sinh\left(\upsilon_n^* z\right)}{\lambda_n a J_0^2\left(\lambda_n\right)}\right]J_1\left(\frac{\lambda_n}{a}r\right) & \text{(type II)}\end{cases}\tag{3.19}$$

As for the tangential velocity u_θ, we can start with Eq. (3.2) and integrate $\int B\mathrm{d}B=\int C_n^2\psi\mathrm{d}\psi$ to obtain

$$B^2=C^2\psi^2+D\quad\text{or}\quad u_\theta=r^{-1}\sqrt{C^2\psi^2+D}\tag{3.20}$$

where D may be dubbed the *tangential surface parameter* as it can be specified by the wall boundary condition imposed on u_θ in Eq. (2.10). Then by inserting ψ into Eq. (3.20), an expanded form of u_θ may be arrived at, specifically

$$ru_\theta = \begin{cases} \left\{ C^2 \left[\sum_{n=0}^{\infty} r \left(\frac{I_L - \cos(\upsilon_n L) I_0}{\lambda_n a J_0^2(\lambda_n)} \frac{\sin(\upsilon_n z)}{\sin(\upsilon_n L)} + \frac{I_0 \cos(\upsilon_n z)}{\lambda_n a J_0^2(\lambda_n)} \right) J_1\left(\frac{\lambda_n}{a} r \right) \right]^2 + D \right\}^{\frac{1}{2}} & \text{(type I)} \\ \left\{ C^2 \left[\sum_{n=0}^{\infty} r \left(\frac{I_L - \cosh(\upsilon_n^* L) I_0}{\lambda_n a J_0^2(\lambda_n)} \frac{\sinh(\upsilon_n^* z)}{\sinh(\upsilon_n^* L)} + \frac{I_0 \cosh(\upsilon_n^* z)}{\lambda_n a J_0^2(\lambda_n)} \right) J_1\left(\frac{\lambda_n}{a} r \right) \right]^2 + D \right\}^{\frac{1}{2}} & \text{(type II)} \end{cases} \tag{3.21}$$

Note that C appears outside the summation due to nonlinearity in the relation between u_θ and ψ. It therefore retains a unique value irrespective of the eigensolutions that are being superimposed in the angular momentum expression given by Eq. (3.21).

3.3 Consolidated Solution

At first glance, the two types of solutions captured in Eqs. (3.18), (3.19), and (3.21) appear dissimilar. Upon further scrutiny, however, we find that one may be restored from the other for $\upsilon_n^2 = i^2(\upsilon_n^*)^2$ or $\upsilon_n = \pm i(\upsilon_n^*)$. This is due to the trigonometric identities

$$\begin{cases} \cosh x = \cos(ix) \\ \sinh x = -i \sin(ix) \end{cases} \quad \text{or} \quad \begin{cases} \cosh \upsilon_n^* = \cos(i\upsilon_n^*) = \cos \upsilon_n \\ \sinh \upsilon_n^* = -i \sin(i\upsilon_n^*) = -i \sin(\pm ii\upsilon_n) = \pm i \sin(\upsilon_n) \end{cases} \tag{3.22}$$

These are needed to switch from the type II to the type I representation, or conversely, through

$$\begin{cases}\cos x=\cosh(ix)\\ \sin x=-i\sinh(ix)\end{cases}\quad\text{or}\quad\begin{cases}\cos\upsilon_n=\cosh(i\upsilon_n)=\cosh(\upsilon_n^*)\\ \sin\upsilon_n=-i\sinh(i\upsilon_n)=-i\sinh(\pm ii\upsilon_n^*)=\pm i\sinh(\upsilon_n^*)\end{cases}\tag{3.23}$$

These identities enable us to confirm by inspection the equality of the two types of solutions obtained for u_θ and u_z. In the interest of clarity, we show how this can be performed for u_r. By substituting $\upsilon_n^*=\pm i\upsilon_n$ into the second member of Eq. (3.19) and using both $\cosh(i\upsilon_n z)=\cos(\upsilon_n z)$ and $\sinh(i\upsilon_n z)=i\sin(\upsilon_n z)$, we have

$$\begin{aligned}u_r&=-\sum_{n=0}^{\infty}\left[\frac{I_L-\cosh(\pm i\upsilon_n L)I_0}{\lambda_n aJ_0^2(\lambda_n)}\frac{(\pm i\upsilon_n)}{\sinh(\pm i\upsilon_n L)}\cosh(\pm i\upsilon_n z)+\frac{I_0}{\lambda_n aJ_0^2(\lambda_n)}(\pm i\upsilon_n)\sinh(\pm i\upsilon_n z)\right]J_1\left(\frac{\lambda_n}{a}r\right)\\&=-\sum_{n=0}^{\infty}\left[\frac{I_L-\cos(\upsilon_n L)I_0}{\lambda_n aJ_0^2(\lambda_n)}\frac{i\upsilon_n}{i\sin(\upsilon_n L)}\cos(\upsilon_n z)+\frac{I_0}{\lambda_n aJ_0^2(\lambda_n)}(i\upsilon_n)i\sin(\upsilon_n z)\right]J_1\left(\frac{\lambda_n}{a}r\right)\end{aligned}\tag{3.24}$$

The outcome is of course identical to the type I representation.

Given that λ_n can vary from 3.8317 to ∞ while C remains fixed, the sign of $C^2-\lambda_n^2/a^2$ can be either positive or negative. Then using the subscript indicial k to denote the largest Bessel root to satisfy $\lambda_k\le aC$, one may identify two subsets that exhibit the following properties

$$\begin{cases}\upsilon_n^2=C^2-\lambda_n^2/a^2\ge 0;\quad \lambda_n\le aC;\quad n=0,\ldots,k\\ (\upsilon_n^*)^2=\lambda_n^2/a^2-C^2>0;\quad \lambda_n>aC;\quad n=k+1,\ldots,\infty\end{cases}\tag{3.25}$$

In each of these subsets, υ_n and υ_n^* remain essentially positive real numbers. Then owing to the identity of the type I and type II expressions, a consolidated formulation may be constructed with no imaginary parts. This is accomplished by taking

$$\psi(r,z)=\sum_{n=0}^{k} r\left[\frac{I_L-\cos(\upsilon_n L)I_0}{\lambda_n a J_0^2(\lambda_n)\sin(\upsilon_n L)}\sin(\upsilon_n z)+\frac{I_0}{\lambda_n a J_0^2(\lambda_n)}\cos(\upsilon_n z)\right]J_1\left(\frac{\lambda_n}{a}r\right)$$

$$+\sum_{n=k+1}^{\infty} r\left[\frac{I_L-\cosh(\upsilon_n^* L)I_0}{\lambda_n a J_0^2(\lambda_n)\sinh(\upsilon_n^* L)}\sinh(\upsilon_n^* z)+\frac{I_0}{\lambda_n a J_0^2(\lambda_n)}\cosh(\upsilon_n^* z)\right]J_1\left(\frac{\lambda_n}{a}r\right) \quad (3.26)$$

Similarly, u_z, u_r and u_θ may be expressed as:

$$u_z=\left\{\begin{array}{l}\displaystyle\sum_{n=0}^{k}\left[\frac{I_L-\cos(\upsilon_n L)I_0}{\lambda_n a J_0^2(\lambda_n)\sin(\upsilon_n L)}\sin(\upsilon_n z)+\frac{I_0\cos(\upsilon_n z)}{\lambda_n a J_0^2(\lambda_n)}\right]\frac{\lambda_n}{a}J_0\left(\frac{\lambda_n}{a}r\right)\\ \displaystyle+\sum_{n=k+1}^{\infty}\left[\frac{I_L-\cosh(\upsilon_n^* L)I_0}{\lambda_n a J_0^2(\lambda_n)\sinh(\upsilon_n^* L)}\sinh(\upsilon_n^* z)+\frac{I_0\cosh(\upsilon_n^* z)}{\lambda_n a J_0^2(\lambda_n)}\right]\frac{\lambda_n}{a}J_0\left(\frac{\lambda_n}{a}r\right)\end{array}\right\} \quad (3.27)$$

$$u_r=\left\{\begin{array}{l}\displaystyle-\sum_{n=0}^{k}\left[\frac{I_L-\cos(\upsilon_n L)I_0}{\lambda_n a J_0^2(\lambda_n)\sin(\upsilon_n L)}\upsilon_n\cos(\upsilon_n z)-\frac{I_0\upsilon_n\sin(\upsilon_n z)}{\lambda_n a J_0^2(\lambda_n)}\right]J_1\left(\frac{\lambda_n}{a}r\right)\\ \displaystyle-\sum_{n=k+1}^{\infty}\left[\frac{I_L-\cosh(\upsilon_n^* L)I_0}{\lambda_n a J_0^2(\lambda_n)\sinh(\upsilon_n^* L)}\upsilon_n^*\cosh(\upsilon_n^* z)+\frac{I_0\upsilon_n^*\sinh(\upsilon_n^* z)}{\lambda_n a J_0^2(\lambda_n)}\right]J_1\left(\frac{\lambda_n}{a}r\right)\end{array}\right\} \quad (3.28)$$

and

$$u_\theta=\left(C^2\left\{\begin{array}{l}\displaystyle\sum_{n=0}^{k}\left[\frac{I_L-\cos(\upsilon_n L)I_0}{\lambda_n a J_0^2(\lambda_n)\sin(\upsilon_n L)}\sin(\upsilon_n z)+\frac{I_0\cos(\upsilon_n z)}{\lambda_n a J_0^2(\lambda_n)}\right]J_1\left(\frac{\lambda_n}{a}r\right)\\ \displaystyle+\sum_{n=k+1}^{\infty}\left[\frac{I_L-\cosh(\upsilon_n^* L)I_0}{\lambda_n a J_0^2(\lambda_n)\sinh(\upsilon_n^* L)}\sinh(\upsilon_n^* z)+\frac{I_0\cosh(\upsilon_n^* z)}{\lambda_n a J_0^2(\lambda_n)}\right]J_1\left(\frac{\lambda_n}{a}r\right)\end{array}\right\}^2+\frac{D}{r^2}\right)^{\frac{1}{2}} \quad (3.29)$$

Equations (3.27), (3.28) and (3.29) constitute the apex of this study and are, therefore, marked as such. To employ this formulation, the arbitrary axial profiles $U_L(r)$ and $U_0(r)$ may be defined based on realistic flow conditions. The specification of u_z at

the endwalls leads to the full determination of the source integrals (I_0, I_l). These affect the expression for u_θ. Nonetheless, two additional parameters remain available to control u_θ and enable us to mimic a realistic tangential velocity at entry. The tangential velocity may be hence prescribed by specifying the constants C and D in a manner to match a given injection function at the endwall $U_\theta(r)$. For example, when $D=0$, a special family of Trkalian flows may be engendered in which no slippage occurs at the sidewall. Conversely, when $D\neq 0$, an essential singularity ascribed to swirl-dominated inviscid flows appears at the centerline. Once C, I_0 and I_l are determined, both u_z and u_r become known throughout the entire domain. Evidently, any velocity pattern imposed at $z=(0,L)$ will have to satisfy volume conservation.

3.4 Normalization

Using standard reference values, one may introduce

$$\begin{cases} \overline{r}=\dfrac{r}{a},\ \overline{z}=\dfrac{z}{a},\ \overline{u}_r=\dfrac{u_r}{U},\ \overline{u}_z=\dfrac{u_z}{U},\ \overline{u}_\theta=\dfrac{u_\theta}{U} \\ \overline{\psi}=\dfrac{\psi}{Ua^2},\ \overline{Q}_i=\dfrac{Q_i}{Ua^2},\ \overline{D}=\dfrac{D}{U^2a^2},\ \overline{C}=Ca,\ \overline{p}=\dfrac{p}{\rho U^2} \end{cases} \tag{3.30}$$

where $\overline{D}$ and $\overline{C}$ represent the non-dimensional forms of the tangential surface parameter and swirl momentum constant, respectively. Implementing the above normalization into our equations, the stream function and velocity expressions become

$$\overline{\psi}(\overline{r},\overline{z})=\sum_{n=0}^{k}\overline{r}\left[\frac{\overline{I}_L-\cos(\overline{\upsilon}_n l)\overline{I}_0}{\lambda_n J_0^2(\lambda_n)\sin(\overline{\upsilon}_n l)}\sin(\overline{\upsilon}_n\overline{z})+\frac{\overline{I}_0}{\lambda_n J_0^2(\lambda_n)}\cos(\overline{\upsilon}_n\overline{z})\right]J_1(\lambda_n\overline{r})$$

$$+\sum_{n=k+1}^{\infty} r\left[\frac{\overline{I}_L-\cosh\left(\overline{\upsilon}_n^*l\right)\overline{I}_0}{\lambda_n J_0^2\left(\lambda_n\right)\sinh\left(\overline{\upsilon}_n^*l\right)}\sinh\left(\overline{\upsilon}_n^*\overline{z}\right)+\frac{\overline{I}_0}{\lambda_n J_0^2\left(\lambda_n\right)}\cosh\left(\overline{\upsilon}_n^*\overline{z}\right)\right]J_1\left(\lambda_n\overline{r}\right) \qquad (3.31)$$

$$\overline{u}_z(\overline{r},\overline{z})=\sum_{n=0}^{k}\left[\frac{\overline{I}_l-\cos\left(\overline{\upsilon}_n l\right)\overline{I}_0}{\lambda_n J_0^2\left(\lambda_n\right)\sin\left(\overline{\upsilon}_n l\right)}\sin\left(\overline{\upsilon}_n\overline{z}\right)+\frac{\overline{I}_0}{\lambda_n J_0^2\left(\lambda_n\right)}\cos\left(\overline{\upsilon}_n\overline{z}\right)\right]\lambda_n J_0\left(\lambda_n\overline{r}\right)$$

$$+\sum_{n=k+1}^{\infty}\left[\frac{\overline{I}_l-\cosh\left(\overline{\upsilon}_n^*l\right)\overline{I}_0}{\lambda_n J_0^2\left(\lambda_n\right)\sinh\left(\overline{\upsilon}_n^*l\right)}\sinh\left(\overline{\upsilon}_n^*\overline{z}\right)+\frac{\overline{I}_0}{\lambda_n J_0^2\left(\lambda_n\right)}\cosh\left(\overline{\upsilon}_n^*\overline{z}\right)\right]\lambda_n J_0\left(\lambda_n\overline{r}\right) \qquad (3.32)$$

$$\overline{u}_r(\overline{r},\overline{z})=-\sum_{n=0}^{k}\left[\frac{\overline{I}_l-\cos\left(\overline{\upsilon}_n l\right)\overline{I}_0}{\lambda_n J_0^2\left(\lambda_n\right)\sin\left(\overline{\upsilon}_n l\right)}\overline{\upsilon}_n\cos\left(\overline{\upsilon}_n\overline{z}\right)-\frac{\overline{I}_0}{\lambda_n J_0^2\left(\lambda_n\right)}\overline{\upsilon}_n\sin\left(\overline{\upsilon}_n\overline{z}\right)\right]J_1\left(\lambda_n\overline{r}\right)$$

$$-\sum_{n=k+1}^{\infty}\left[\frac{\overline{I}_l-\cosh\left(\overline{\upsilon}_n^*l\right)\overline{I}_0}{\lambda_n J_0^2\left(\lambda_n\right)\sinh\left(\overline{\upsilon}_n^*l\right)}\overline{\upsilon}_n^*\cosh\left(\overline{\upsilon}_n\overline{z}\right)+\frac{\overline{I}_0}{\lambda_n J_0^2\left(\lambda_n\right)}\overline{\upsilon}_n^*\sinh\left(\overline{\upsilon}_n^*\overline{z}\right)\right]J_1\left(\lambda_n\overline{r}\right) \qquad (3.33)$$

and, for the tangential component,

$$\overline{u}_\theta(\overline{r},\overline{z})=\left(\overline{C}^2\left\{\sum_{n=0}^{k}\left[\frac{\overline{I}_l-\cos\left(\overline{\upsilon}_n l\right)\overline{I}_0}{\lambda_n J_0^2\left(\lambda_n\right)\sin\left(\overline{\upsilon}_n l\right)}\sin\left(\overline{\upsilon}_n\overline{z}\right)+\frac{\overline{I}_0}{\lambda_n J_0^2\left(\lambda_n\right)}\cos\left(\overline{\upsilon}_n\overline{z}\right)\right]J_1\left(\lambda_n\overline{r}\right)\right.\right.$$

$$\left.\left.+\sum_{n=k+1}^{\infty}\left[\frac{\overline{I}_l-\cosh\left(\overline{\upsilon}_n^*l\right)\overline{I}_0}{\lambda_n J_0^2\left(\lambda_n\right)\sinh\left(\overline{\upsilon}_n^*l\right)}\sinh\left(\overline{\upsilon}_n^*\overline{z}\right)+\frac{\overline{I}_0}{\lambda_n J_0^2\left(\lambda_n\right)}\cosh\left(\overline{\upsilon}_n^*\overline{z}\right)\right]J_1\left(\lambda_n\overline{r}\right)\right\}^2+\frac{\overline{D}}{\overline{r}^2}\right)^{\frac{1}{2}} \qquad (3.34)$$

Here the normalized source integrals may be evaluated from

$$\begin{cases}\overline{I}_l\equiv 2\int_0^1\overline{u}_z(\overline{r},l)\overline{r}J_0\left(\lambda_n\overline{r}\right)\mathrm{d}\overline{r} & \text{(endwall)}\\ \overline{I}_0\equiv 2\int_0^1\overline{u}_z(\overline{r},0)\overline{r}J_0\left(\lambda_n\overline{r}\right)\mathrm{d}\overline{r} & \text{(headwall)}\end{cases} \qquad (3.35)$$

where $\overline{\upsilon}_n^2=\overline{C}^2-\lambda_n^2$ and $(\overline{\upsilon}_n^*)^2=\lambda_n^2-\overline{C}^2$. It may be instructive to note that the foregoing solution can accommodate arbitrary headwall and endwall velocity patterns, $\overline{u}_z(\overline{r},0)$ and

$\bar{u}_z(\bar{r},l)$, so long as the imposed profiles remain observant of the mass conservation principle. Otherwise, the solution initiated with an incongruent model will be self-corrected in the resulting series representation that produces a distribution which, when evaluated at the endwalls, will generate a velocity profile that is different from the one originally imposed. The altered profile at the boundary will strongly resemble the one prescribed as an input except for some minor differences that cause it to gracefully satisfy mass conservation. Conversely, when a physical solution that observes continuity is imposed at the endwalls, the resulting series summation will return the same profile as the input source. Such self-correcting behavior is quite interesting to note in the present model. It may be ascribed to the series solution being analytic, continuous and infinitely differentiable, in addition to being consistent with mass conservation throughout the entire chamber. These properties instill in our solution an aversion towards unphysical jumps, especially at its boundaries.

3.5 Vorticity

Another quantity that is of vital interest in fluid flows is the vorticity. By definition, vorticity can be calculated through

$$\bar{\boldsymbol{\omega}} = \nabla \times \bar{\boldsymbol{u}} \tag{3.36}$$

Given the components of $\bar{\boldsymbol{u}}$ defined in Eqs. (3.32), (3.33) and (3.34), the vorticity can be readily found viz.

$$\bar{\omega}_r = -\frac{\bar{C}^2}{\bar{r}\sqrt{\bar{C}^2\bar{\psi}^2 + \bar{D}}}\bar{\psi}\frac{\partial\bar{\psi}}{\partial\bar{z}} \tag{3.37}$$

where $\bar{\psi}$ is defined in Eq. (3.31) and

$$\frac{\partial \bar{\psi}(\bar{r},\bar{z})}{\partial z} = \sum_{n=0}^{k} \bar{r}\left[\frac{\bar{I}_L - \cos(\bar{\upsilon}_n l)\bar{I}_0}{\lambda_n J_0^2(\lambda_n)\sin(\bar{\upsilon}_n l)}\bar{\upsilon}_n \cos(\bar{\upsilon}_n \bar{z}) - \frac{\bar{I}_0}{\lambda_n J_0^2(\lambda_n)}\bar{\upsilon}_n \sin(\bar{\upsilon}_n \bar{z})\right] J_1(\lambda_n \bar{r})$$

$$+ \sum_{n=k+1}^{\infty} r\left[\frac{\bar{I}_L - \cosh(\bar{\upsilon}_n^* l)\bar{I}_0}{\lambda_n J_0^2(\lambda_n)\sinh(\bar{\upsilon}_n^* l)}\bar{\upsilon}_n^* \cosh(\bar{\upsilon}_n^* \bar{z}) + \frac{\bar{I}_0}{\lambda_n J_0^2(\lambda_n)}\bar{\upsilon}_n^* \sinh(\bar{\upsilon}_n^* \bar{z})\right] J_1(\lambda_n \bar{r}) \qquad (3.38)$$

For the tangential component of vorticity, we have

$$\bar{\omega}_\theta = \frac{\bar{C}^2 \bar{\psi}}{\bar{r}} \qquad (3.39)$$

Similarly, the axial component may be obtained from

$$\bar{\omega}_z = \frac{\bar{C}^2}{\bar{r}\sqrt{\bar{C}^2\bar{\psi}^2 + \bar{D}}}\bar{\psi}\frac{\partial \bar{\psi}}{\partial \bar{r}} \qquad (3.40)$$

where

$$\frac{\partial \bar{\psi}}{\partial \bar{r}} = \sum_{n=0}^{k}\left[\frac{\bar{I}_L - \cos(\bar{\upsilon}_n l)\bar{I}_0}{\lambda_n J_0^2(\lambda_n)\sin(\bar{\upsilon}_n l)}\sin(\bar{\upsilon}_n \bar{z}) + \frac{\bar{I}_0 \cos(\bar{\upsilon}_n \bar{z})}{\lambda_n J_0^2(\lambda_n)}\right]\left\{J_1(\lambda_n \bar{r}) + \tfrac{1}{2}\bar{r}[J_0(\lambda_n \bar{r}) - J_2(\lambda_n \bar{r})]\right\}$$

$$+ \sum_{n=k+1}^{\infty}\left[\frac{\bar{I}_L - \cosh(\bar{\upsilon}_n^* l)\bar{I}_0}{\lambda_n J_0^2(\lambda_n)\sinh(\bar{\upsilon}_n^* l)}\sinh(\bar{\upsilon}_n^* \bar{z}) + \frac{\bar{I}_0 \cosh(\bar{\upsilon}_n^* \bar{z})}{\lambda_n J_0^2(\lambda_n)}\right]\left\{J_1(\lambda_n \bar{r}) + \tfrac{1}{2}\bar{r}[J_0(\lambda_n \bar{r}) - J_2(\lambda_n \bar{r})]\right\} \qquad (3.41)$$

At length, the total vorticity magnitude can be defined as

$$\bar{\omega} = \sqrt{\bar{\omega}_z^2 + \bar{\omega}_\theta^2 + \bar{\omega}_r^2} = \frac{\bar{C}^2\bar{\psi}}{\bar{r}}\sqrt{\frac{1}{\bar{C}^2\bar{\psi}^2 + \bar{D}}\left[\left(\frac{\partial \bar{\psi}}{\partial \bar{r}}\right)^2 + \left(\frac{\partial \bar{\psi}}{\partial \bar{r}}\right)^2 + \bar{C}^2\bar{\psi}^2 + \bar{D}\right]} \qquad (3.42)$$

The evaluation of Eq. (3.42) is best relegated to a symbolic program such as Mathematica [40].

3.6 Pressure Distribution

The pressure distribution can be directly obtained from the Euler equations, specifically

$$\overline{u}_r \frac{\partial \overline{u}_z}{\partial \overline{r}} + \overline{u}_z \frac{\partial \overline{u}_z}{\partial \overline{z}} = -\frac{\partial \overline{p}}{\partial \overline{z}} \tag{3.43}$$

$$\overline{u}_r \frac{\partial \overline{u}_r}{\partial \overline{r}} - \frac{\overline{u}_\theta^2}{\overline{r}} + \overline{u}_z \frac{\partial \overline{u}_r}{\partial \overline{z}} = -\frac{\partial \overline{p}}{\partial \overline{r}} \tag{3.44}$$

where the velocities are provided through Eqs. (3.32), (3.33) and (3.34). Integrating the product of the velocities will lead to terms of the form

$$\int J_k(mr) J_l(nr) \mathrm{d}r \tag{3.45}$$

which do not exhibit any known analytical solution. However, an exact mathematical solution can be found by taking only the first term in the series summation of the velocities. At the outlet, one finds

$$\begin{aligned} \Delta\overline{p} = {} & \frac{1}{4}\overline{K}_1^2 \lambda_0^2 J_0^2(\lambda_0 \overline{r})\left[\cos(2\overline{\upsilon}_0 \overline{z}) - 1\right] \\ & + \frac{1}{4}\overline{K}_1^2 \lambda_0^2 J_1^2(\lambda_0 \overline{r})\left[\cos(2\overline{\upsilon}_0 \overline{z}) + 1\right] - \frac{1}{2} C^2 \overline{K}_1^2 J_1^2(\lambda_0 \overline{r}) - \frac{\overline{D}}{2\overline{r}^2} + C_0 \end{aligned} \tag{3.46}$$

where $\overline{K}_1$ is defined as

$$\overline{K}_1 = \frac{\overline{I}_l - \cos\left(\overline{\upsilon}_0 l\right)\overline{I}_0}{\lambda_0 J_0^2\left(\lambda_0\right)\sin\left(\overline{\upsilon}_0 l\right)} \tag{3.47}$$

and λ_0 is the first root of the Bessel function of the first kind.

The reference pressure is taken to be at the line of intersection between the headwall and sidewall ($\overline{r} = 1$ and $\overline{z} = 0$) as stated in Eq. (2.11). This enables us to extract

$$C_0 = \frac{\bar{D}}{2} \tag{3.48}$$

and so

$$\Delta\bar{p} = \frac{1}{4}\bar{K}_1^2\lambda_0^2 J_0^2(\lambda_0\bar{r})\left[\cos(2\bar{\upsilon}_0\bar{z}) - 1\right]$$

$$+\frac{1}{4}\bar{K}_1^2\lambda_0^2 J_1^2(\lambda_0\bar{r})\left[\cos(2\bar{\upsilon}_0\bar{z}) + 1\right] - \frac{1}{2}\bar{C}^2\bar{K}_1^2 J_1^2(\lambda_0\bar{r}) + \frac{\bar{D}}{2}\left(1 - \frac{1}{\bar{r}^2}\right) \tag{3.49}$$

To find the pressure while keeping more than one term from the velocity formulation, numerical methods or series approximations can be used to solve the integrals similar to Eq. (3.45).

Finally, before leaving this chapter, we note that the velocity at the headwall $U_0(r)$ will be set to zero in the majority of cases due to our primary interest in modeling a vortex chamber with a closed headwall, thus mimicking a non-reactive cyclonic motion in a cylindrical chamber.

Chapter 4

Characterization of the Inviscid Solution

A systematic approach should be followed in order to apply the newly developed velocity equations. The steps are summarized by the following:

a) Specifying the axial velocity profiles at the headwall and endwall ($\bar{U}_0$ and $\bar{U}_l$).

b) Setting the tangential surface parameter $\bar{D}$ to match the sidewall tangential velocity at $\bar{z} = l$.

$$\sqrt{\bar{D}} = \bar{U}_\theta(1) \tag{4.1}$$

c) Identifying the swirl momentum constant $\bar{C}$ such that $\bar{u}_\theta$ at the endwall matches $\bar{U}_\theta(r)$. Since the relation is highly nonlinear, one can resolve to the method of least squares to find $\bar{C}$.

Several analytical models for the cold bidirectional vortex engine can be found in the literature. The most prominent of these are listed in Table 4-1. Note that none of these models incorporate secondary injection (e.g. fuel) at the headwall. In order to mimic the no-head injection scenario in our model, the headwall velocity $U_0(r)$ will be set to zero. Conversely, the endwall velocity $U_L(r)$ will be set equal to the axial profile at the inlet boundary of the model to be examined.

4.1 Axial Velocity

Our procedure consists of using the boundary conditions at the endwalls to fix the inlet and outlet axial velocities, before selecting the independent parameters, $\bar{C}$ and $\bar{D}$, in such a way to reproduce, as closely as possible, the desired tangential velocity at $\bar{z} = l$. The resulting formulation can then be employed to evaluate the axial velocity over the entire chamber domain, including the endwall boundaries, where a verification of the input profile imposed initially may be undertaken. To illustrate this process, the profiles posted in Table 4-1 are chosen as benchmarks. Using their endwall values at $\bar{z} = l$ as inflow requirements in Eq. (3.32), the ensuing description for $\bar{u}_z$ may be readily obtained.

Corresponding results are displayed in Figure 4-1a and Figure 4-2a for the linear and nonlinear profiles respectively. These are given at several axial stations extending from the headwall to the endwall. The axial solutions produced directly from Majdalani [13] without series summations are shown on the right-hand-side part (b) of the same graphs. These happen to be identical for the Beltramian and Trkalian configurations. It

Table 4-1. Analytical models for the bidirectional vortex in a confined cylindrical chamber

Model	Velocity Profile
Complex-Lamellar [32]	$\overline{\boldsymbol{u}} = -\dfrac{\sin(\pi\overline{r}^2)}{2\pi\sigma l\sin(\pi\beta^2)}\mathbf{e_r} + \dfrac{1}{\overline{r}}\mathbf{e_\theta} + \dfrac{\overline{z}\cos(\pi\overline{r}^2)}{\sigma l\sin(\pi\beta^2)}\mathbf{e_z}$
Linear Beltramian [13]	$\overline{\boldsymbol{u}} = -c\kappa J_1(\lambda_0\overline{r})\mathbf{e_r} + \dfrac{1}{\overline{r}}\sqrt{1+c^2\lambda_0^2\kappa^2\overline{r}^2\overline{z}^2J_1^2(\lambda_0\overline{r})}\mathbf{e_\theta} + c\lambda_0\kappa\overline{z}J_0(\lambda_0\overline{r})\mathbf{e_z}$
Linear Trkalian [13]	$\overline{\boldsymbol{u}} = -c\kappa J_1(\lambda_0\overline{r})\mathbf{e_r} + c\lambda_0\kappa\overline{z}J_1(\lambda_0\overline{r})\mathbf{e_\theta} + c\lambda_0\kappa\overline{z}J_0(\lambda_0\overline{r})\mathbf{e_z}$
Nonlinear Beltramian [13]	$\overline{\boldsymbol{u}} = -\frac{1}{2}\pi c\kappa\cos(\frac{1}{2}\pi\overline{z}/l)J_1(\lambda_0\overline{r})\mathbf{e_r} + c\lambda_0\kappa l\sin(\frac{1}{2}\pi\overline{z}/l)J_0(\lambda_0\overline{r})\mathbf{e_z}$ $+\dfrac{1}{\overline{r}}\sqrt{1+c^2\kappa^2(\lambda_0^2l^2+\frac{1}{4}\pi^2)\overline{r}^2J_1^2(\lambda_0\overline{r})\sin^2(\frac{1}{2}\pi\overline{z}/l)}\mathbf{e_\theta}$
Nonlinear Trkalian [13]	$\overline{\boldsymbol{u}} = -\frac{1}{2}\pi c\kappa\cos(\frac{1}{2}\pi\overline{z}/l)J_1(\lambda_0\overline{r})\mathbf{e_r} + c\lambda_0\kappa l\sin(\frac{1}{2}\pi\overline{z}/l)J_0(\lambda_0\overline{r})\mathbf{e_z}$ $+\frac{1}{2}\pi c\kappa\sqrt{1+4\lambda_0^2l^2/\pi^2}\sin(\frac{1}{2}\pi\overline{z}/l)J_1(\lambda_0\overline{r})\mathbf{e_\theta}$

can be seen that the present model regenerates the same outcome as before in both flow configurations. The striking resemblance observed in these illustrations may be attributed to the two analyses being based on analogous approximations and assumptions at their points of departure, including their reliance on a linear BHE and a consistent set of physical requirements. Furthermore, the eigenvalue λ_0 used by Majdalani [13] in defining the aforementioned cases belongs to the subset of eigenvalues that are built into the generalized framework developed here.

To further visualize the behavior of Eq. (3.32), $\overline{u}_z$ is presented in Figure 4-3 where it is compared to the Complex-Lamellar counterpart constructed by Vyas and Majdalani [32]. Unlike the Vyas-Majdalani motion in which the axial velocity along the centerline (or sidewall) increases (or decreases) linearly with the distance from the headwall, the acceleration associated with the present model is spatially variant. As it may be inferred from Figure 4-3a, the axial variation of $\overline{u}_z$ follows a nonlinear trend, in contrast to the linear behavior of the Complex-Lamellar solution. This may be attributed to the latter originating from a different BHE formulation than the one utilized here.

The axial velocities in the figures above are combined with two flow parameters κ and σ. We recall that $\kappa = (2\pi\sigma l)^{-1}$ is the tangential inflow parameter as defined by Majdalani [13] whereas $\sigma = a^2 / A_i$ is the swirl number introduced by Vyas and Majdalani [32]. These parameters are included in this study to be consistent in comparing results to other models.

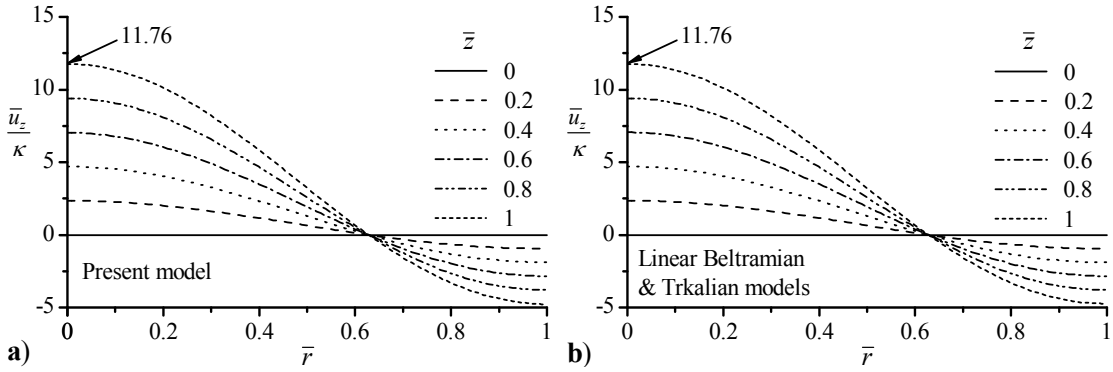

Figure 4-1. Comparison between axial velocities corresponding to a) Eq. (3.32) and b) the linear Beltramian and Trkalian formulations obtained by Majdalani [13]. Here $l = 1$.

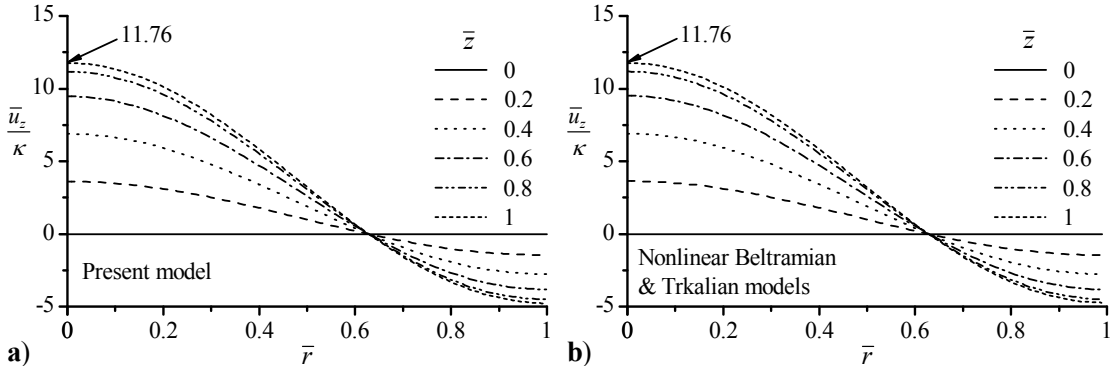

Figure 4-2. Comparison between axial velocities corresponding to a) Eq. (3.32) and b) the nonlinear Beltramian and Trkalian formulations obtained by Majdalani [13]. Here $l = 1$.

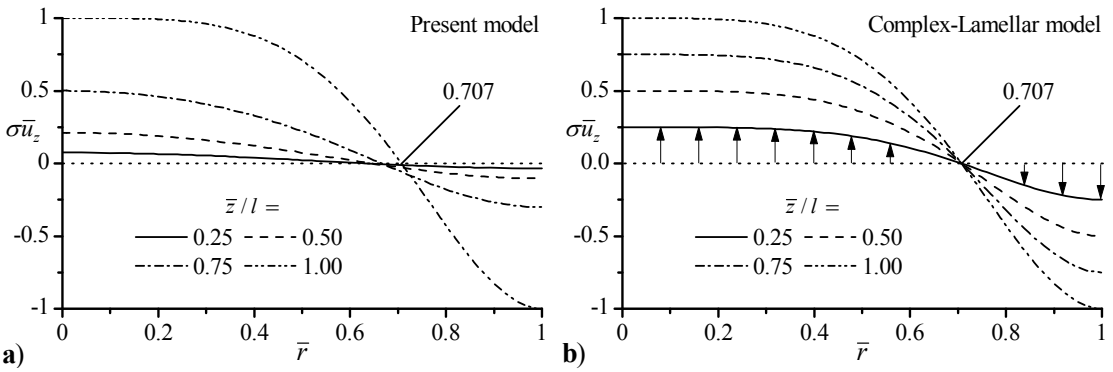

Figure 4-3. Comparison between the axial velocities corresponding to a) Eq. (3.32) and b) the Complex-Lamellar solution.

4.2 Mantle Location

The mantle location in a bidirectional vortex is the radial position separating the outer swirl from the inner vortex. At that virtual boundary, the axial component of velocity vanishes.

Returning to Figure 4-3b, a fixed locus of the mantle may be seen at $\bar{r} = 0.707$, a key characteristic of the Complex-Lamellar model, irrespective of the axial position. Conversely, the location of the series approximation in Figure 4-3a is seen to slightly shift along the axis of the chamber, starting from $\bar{r} = 0.707$ at $\bar{z} = l$, where the simulated profile is imposed, to a value approaching 0.63 that is characteristic of both Beltramian and Trkalian solutions further downstream. The numerical values are shown in Table 4-2. The variability displayed by the analytical model is similar to the physical behavior reported in the experiments by Smith [26, 27]. Therein, the mantle is shown to vary in one case from $\bar{r} = 0.583$ to 0.663 while traversing 10.7 inches of chamber length, and in the other, from $\bar{r} = 0.708$ to 0.721 while using a different vortex finder and Reynolds

Table 4-2. Mantle location obtained using the Complex-Lamellar endwall profile

Location	$\bar{z}/l$	$\bar{r}$
1	0.25	0.637
2	0.5	0.645
3	0.75	0.665
4	1	0.707
Mean		**0.6635**

number. In the first case, the mantle shifts towards the chamber wall as it approaches the exit, whereas in the second case, it shifts inwardly towards the core. This shows that the mantle varies throughout the length of the chamber in order to more suitably match the exit boundary diameter, and as it moves away from that boundary, it relaxes to a natural mantle location that is shown to be approximately 0.63 in the present analysis. Incidentally, Hoekstra, Derksen and van den Akker [28] also reported in their numerical study the location of zero axial velocity to be around $\bar{r} \approx 0.675$.

4.3 Tangential Velocity

The tangential velocity at $\bar{z} = l$ is dependent on the choice of $U_\theta(r)$. The two constants C and D lend us two degrees of freedom by providing two parameters that can be adjusted to the extent of accounting for different tangential velocity profiles at the endwalls. To demonstrate the flexibility of our solution, we consider the nonlinear Beltramian and Trkalian axial profiles by Majdalani [13], where each model features a different tangential velocity at the inlet.

Figure 4-4a is based on Eq. (3.34) using Majdalani's slip-resistant Trkalian profile [13] in the axial direction. In this case, we set $\overline{D} = 0$ in the tangential velocity expression in order to ensure that it vanishes at $\overline{r} = 1$. We then adjust the parameter $\overline{C}$ to match the magnitude of $\overline{u}_\theta$ at the endwall. Because the inlet tangential speed observes the no-slip requirement at the sidewall, the velocity-adherence property is maintained along the entire length of the wall. For example, it can be seen that $\overline{u}_\theta$ at $\overline{r} = 1$ vanishes for $0 \le \overline{z} \le l$. Evidently such will not be the behavior under different inlet conditions, especially when using motions that permit slip at the sidewall.

Our second test case provides an illustration of the latter situation. Now we use the linearly varying Beltramian profile with a slip permitting tangential velocity at $\overline{z} = l$. The corresponding $\overline{u}_\theta(\overline{r}, l)$ displays a hyperbolic relation with the radial distance, thus causing $\overline{u}_\theta$ to approach a nonzero value at the sidewall and infinity at the centerline. In our effort at matching this free-vortex motion, both $\overline{C}$ and $\overline{D}$ are carefully selected. The resulting solution in Figure 4-5a displays incremental shifts in the tangential velocity at different axial positions. This velocity shows a slight dependence on the axial position, with this dependence being concentrated in the region between $0.3 \le \overline{r} \le 0.8$ roughly.

Such behavior for the Trkalian and Beltramian inputs is identical to the one reported by Majdalani [13] which is presented alongside the plots of Eq. (3.34) in Figure 4-4b and Figure 4-5b.

Back to the Complex-Lamellar model, its tangential velocity remains $1/\overline{r}$ throughout the length of the chamber. It is independent of the axial position. In the

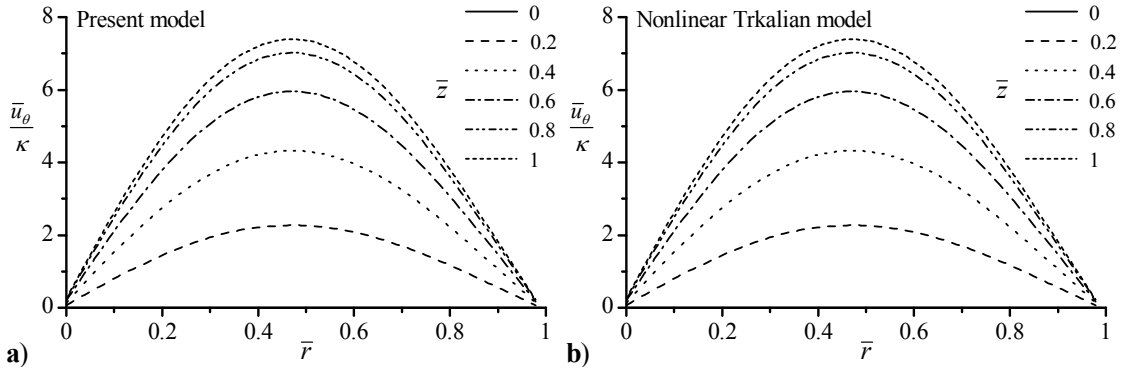

Figure 4-4. Comparison between tangential velocities corresponding to a) Eq. (3.34)and b) the nonlinear Trkalian formulations obtained by Majdalani [13]. Here $l = 1$ and $\kappa = 0.125$.

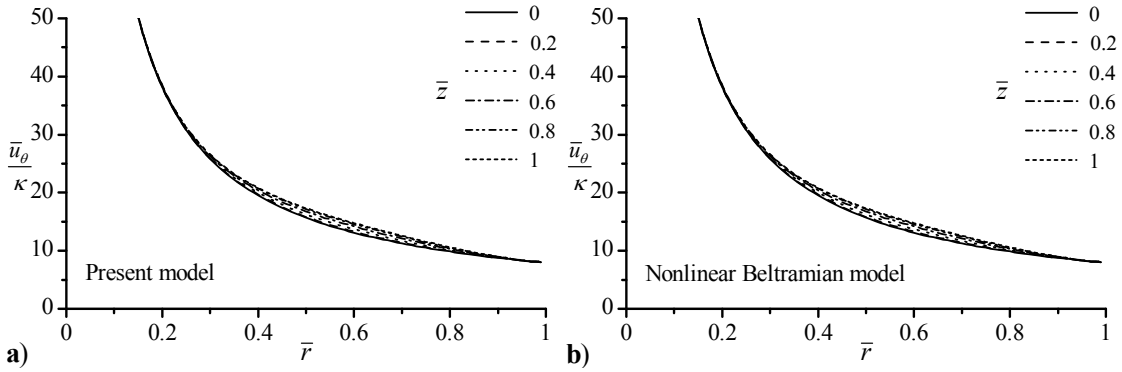

Figure 4-5. Comparison between tangential velocities corresponding to a) Eq. (3.34)and b) the nonlinear Beltramian formulations obtained by Majdalani [13]. Here $l = 1$ and $\kappa = 0.125$.

present solution, matching the boundary condition at the endwall leads to $\bar{C} = 0$ and $\bar{D} = 1$, thus reducing Eq. (3.34) to $\bar{u}_\theta = 1/\bar{r}$, which corresponds to the Complex-Lamellar model.

4.4 Radial Velocity

The radial velocity in all of the models considered vanishes at the centerline due to axial symmetry. Furthermore, unlike simulated solid or hybrid rocket chambers, the vortex-fired rocket engines do not exhibit any radial velocity along the sidewall. In constructing our solution, the radial velocity profile does not appear explicitly in the inflow/outflow integrals of Eq. (3.33) and, as such, is not specifically imposed at the sidewall. Nonetheless, our results show that the radial velocity predicted by the series approximation along the inlet is strikingly similar to the profile that it seeks to mimic. This outcome may be attributed to $\bar{u}_z$ and $\bar{u}_r$ being intimately linked through the axisymmetric continuity relation, and this connection remains independent of the tangential velocity. So by imposing $\bar{u}_z$ at the boundary, we are implicitly securing its unique companion $\bar{u}_r$ at the same location.

The radial velocities corresponding to the linear Beltramian, nonlinear Beltramian and the Complex-Lamellar inputs are plotted in Figure 4-6a, b and c, respectively. Each model suggests a different behavior. This component describes the quantity of fluid that is traversing from the outer to the inner vortex. Therefore it is important to understand how deep a particle penetrates into the cyclone before switching directions. In the

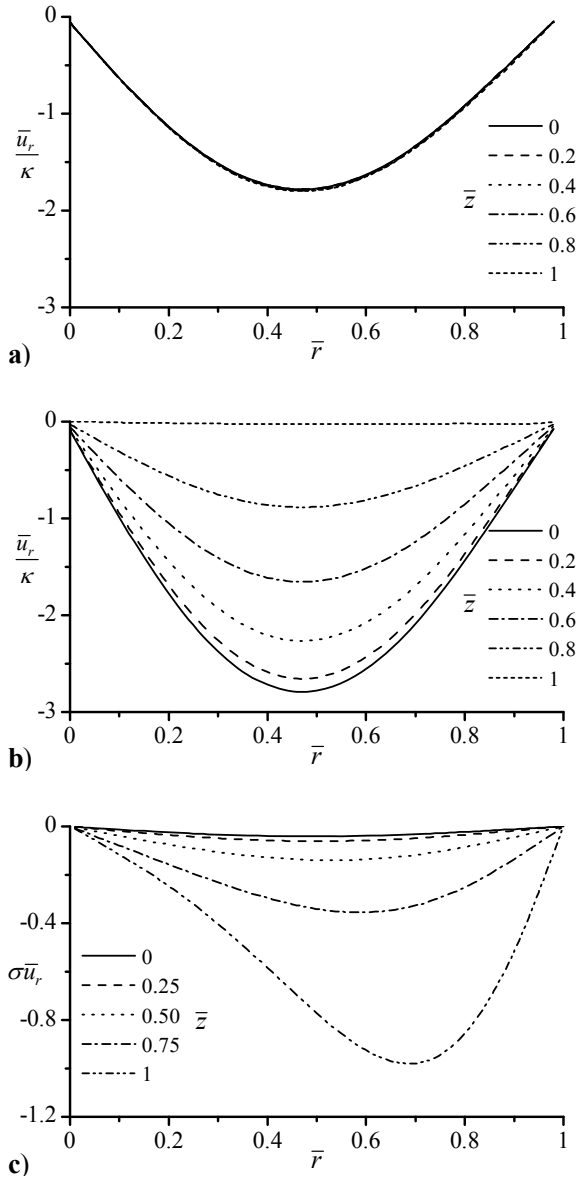

Figure 4-6. Comparison between radial velocities corresponding to Eq. (3.33) for a) linear Beltramian, b) nonlinear Beltramian and c) Complex-Lamellar input profiles.

Complex-Lamellar case, most of the fluid moves inwardly in the vicinity of the inlet. The nonlinear Beltramian profile is accompanied by deeper penetration of the rotational particles. Since all three inputs have the same tangential surface parameter $\overline{D}$, the swirl momentum constant $\overline{C}$ is what controls this particular flow feature. It turns out that $\overline{C}$ is also a direct measure of the vorticity that is being introduced into the system at the boundary, as it can be seen from Eqs. (3.37), (3.39) and (3.40). The more vorticity is acquired at the endwall through the distribution of the tangential velocity $U_\theta(r)$, the more the fluid deformation and penetration of fluid elements will be engendered as the flow enters the chamber before switching direction and returning through the inner vortex.

4.5 Vorticity

In order to mimic the Complex-Lamellar tangential velocity in the input plane, $\overline{C}$ is set to zero, thus causing the flow to become potential. This is not the case for the linear and nonlinear Beltramian motions. From Eq. (3.42), one can reproduce the vorticity distribution shown in Figure 4-7a and b for aspect ratios of $l = 2$ and for the two input models. Our flow is symmetrical about the chamber axis, and so it is sufficient to plot fluid trajectories in two dimensions over $0 \le \overline{r} \le 1$ and $0 \le \overline{z} \le l$.

Since the model is inviscid, no vorticity is generated inside the chamber. All of the vorticity flows through the boundary. This explains the fact that most vorticity remains concentrated near the endwall and as we move deeper into the chamber, vorticity decreases. It reaches zero at the headwall and sidewall.

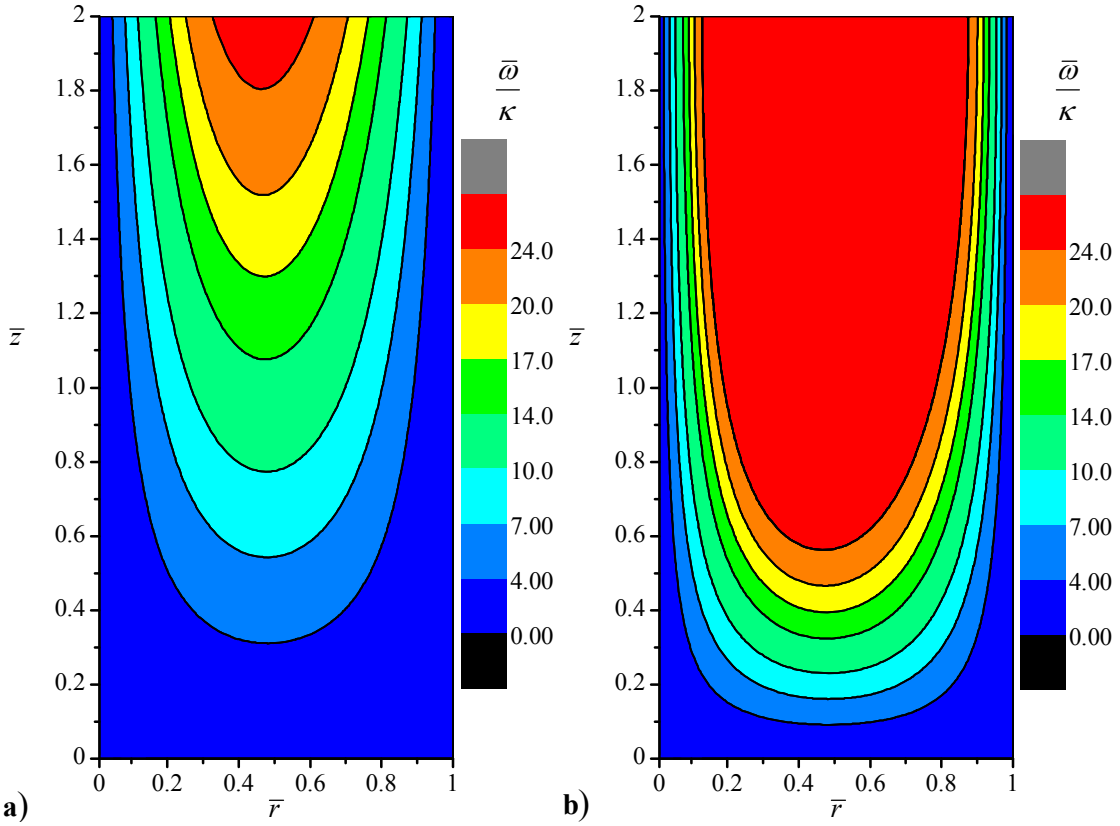

Figure 4-7. Vorticity distribution of Eq. (3.42) for a) linear Beltramian and b) nonlinear Beltramian inputs. Here $l = 2$.

As stated in the previous section, vorticity controls the penetration depth of rotational particles before transferring into the inner vortex. For the application to vortex engines, the oxidizer is required to approach the endwall where the fuel is injected. The leakage from the outer to the inner vortex along the length of the chamber will decrease the efficiency of the engine. Therefore, it is favorable to increase the vorticity in the inlet plane. From this perspective, the nonlinear Beltramian model may be viewed as more favorable than the other models.

4.6 Pressure Distribution

The pressure reference is taken to be at the intersection between the headwall and sidewall as stated earlier. This can be seen in Figure 4-8 where the pressure at $\overline{r} = 1$ and $\overline{z} = 0$ is zero in all cases.

The pressure decreases in the radial direction as we move away from the sidewall towards the core. For the axial direction, the pressure variations are imperceptible except for the Trkalian cases where the pressure decreases going towards the exit plane. These results are consistent with the original models by Majdalani [13] and Vyas and Majdalani [32]. The Beltramian and Complex-Lamellar models exhibit a singularity at the centerline. The difference in pressure reaches negative infinity. This is attributed to the infinitely increasing azimuthal velocities in these models. Physically, this singularity is not only expected, but in fact seems to characterize most inviscid swirling flows in which viscosity is not accounted for near the axis of rotation [22]. In the next chapter, it will be shown how this singularity may be overcome by introducing viscosity to the system.

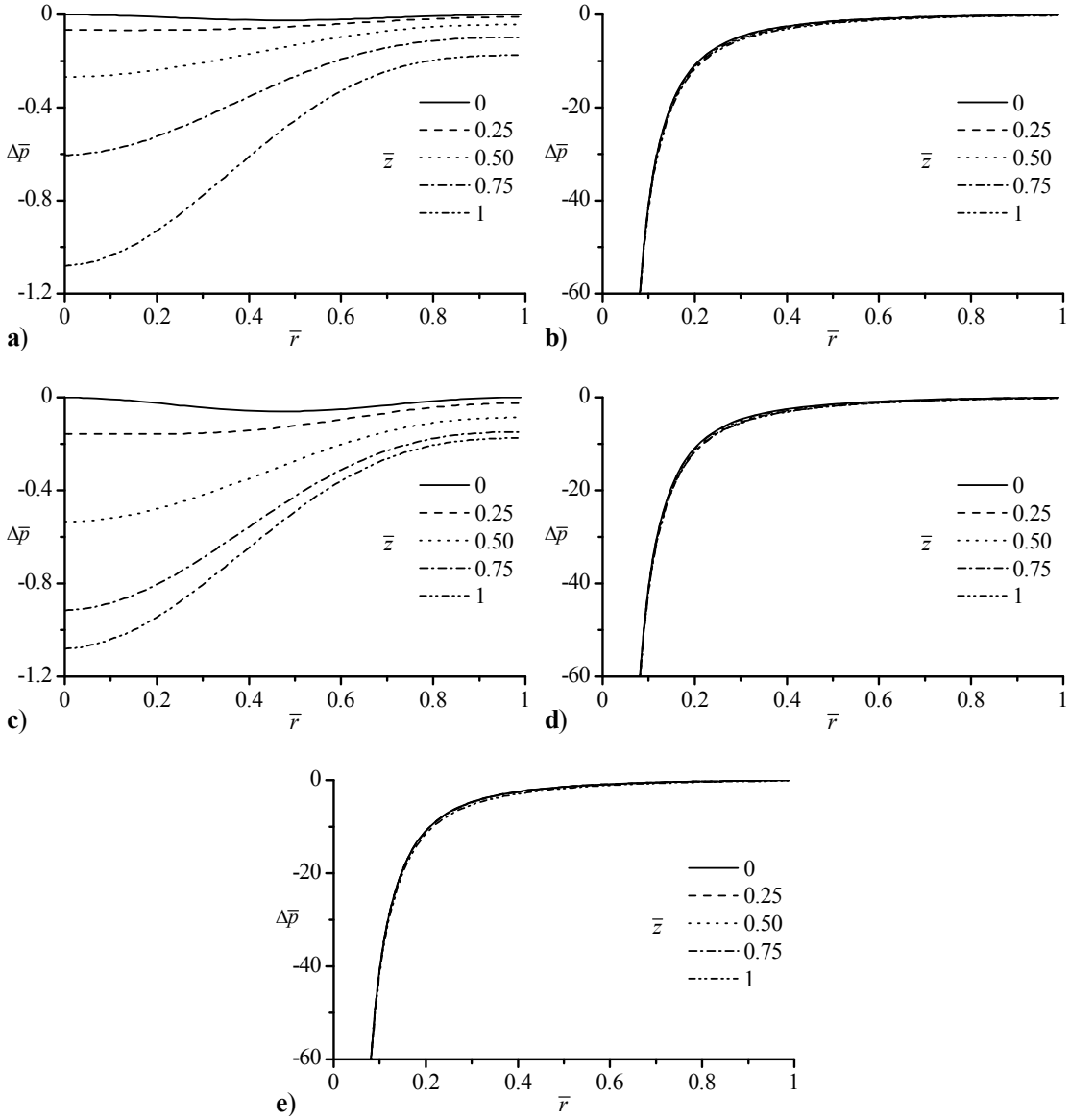

Figure 4-8. Radial distribution of the pressure based on Eq. (3.49) with boundary conditions from a) linear Trkalian, b) linear Beltramian, c) nonlinear Trkalian, d) nonlinear Beltramian and e) Complex-Lamellar models.

It should be remarked that Eq. (3.46) was derived using only one term of the velocity summation. Figure 4-9 provides a plot of a three-term pressure approximation compared to the one-term result. Only small discrepancies can be detected between the two representations. A careful study of the velocity equations shows that the magnitude of the first term $(n = 1)$ is by far the largest, making a one-term approximation suitable for the pressure.

The three-term pressure was calculated using series approximations. Higher levels of accuracy can be found using similar methods but these are not presented here for brevity.

4.7 Headwall Velocities

So far, all the cases presented have assumed a rigid wall at the headwall

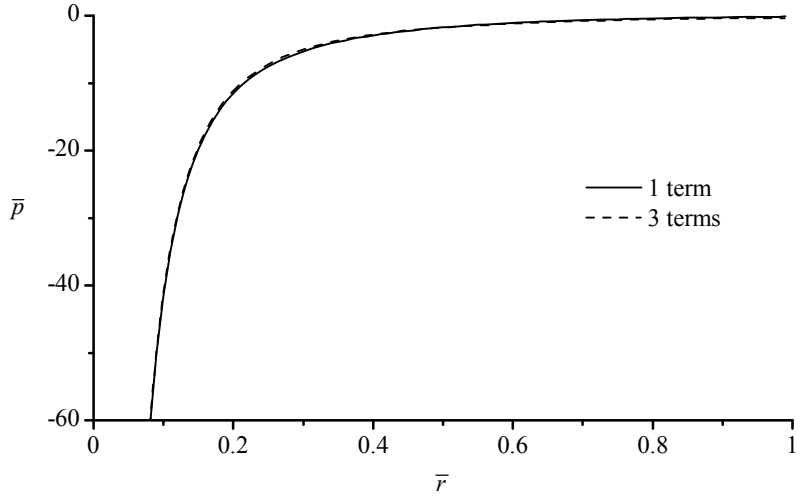

Figure 4-9. Radial distribution of a one-term and three-term pressure at $\bar{z} = l$.

boundary. Mathematically, this is done by setting $U_0 = 0$. To demonstrate the capability of the velocity equations to cope with arbitrary injections at both ends of the domain, two cases will be presented where the headwall velocity will be set to a nonzero value.

4.7.1 Reverse Chamber

In this section, the endwall is considered to be a closed rigid wall with $U_L = 0$. At the headwall, a nonlinear Beltramian profile is set. Note that the sign of the imposed profile has been reversed because, at the lower boundary, fluid exiting the chamber has a

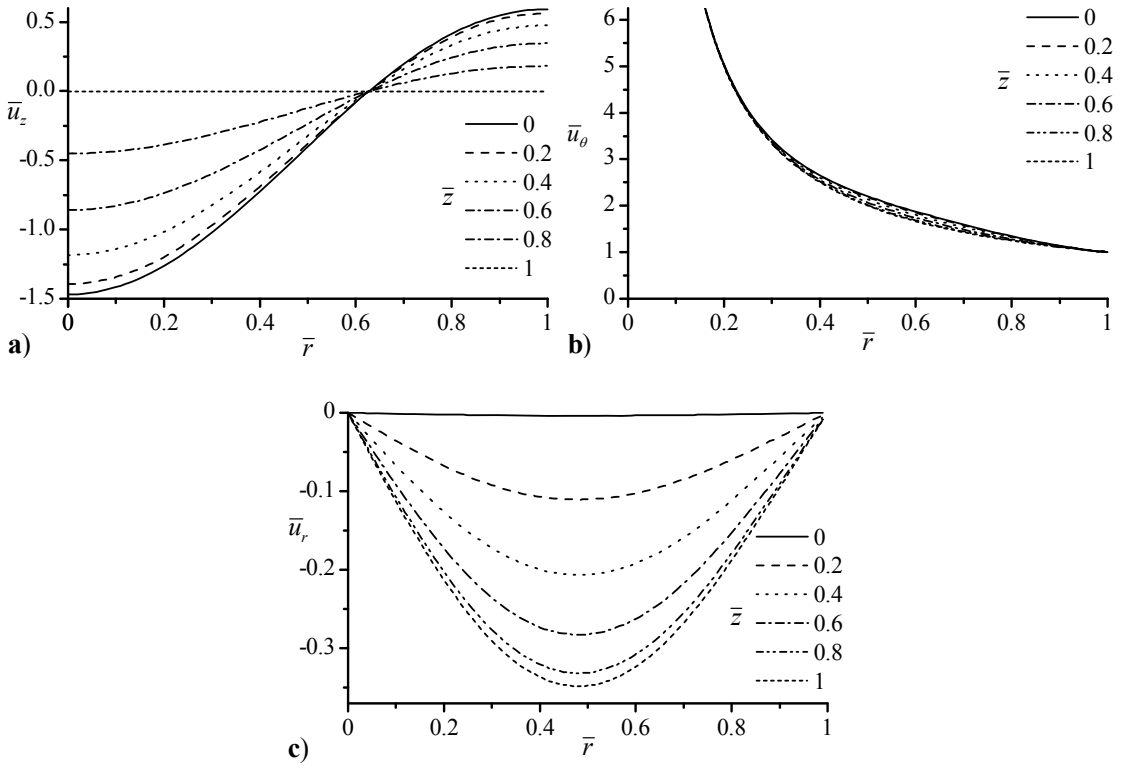

Figure 4-10. Radial distribution of the a) axial, b) tangential and c) radial velocities in a reversed chamber.

negative velocity.

Figure 4-10 shows the velocity distribution inside the vortex chamber. In part "a", the axial velocity matches the imposed profile at the headwall. The velocity then decreases until it reaches zero at the endwall to match the profile prescribed at this boundary. A close comparison of Figure 4-10a with Figure 4-2a shows the same distribution of the axial velocity in which the boundaries at $\bar{z} = l$ and $\bar{z} = 0$ are interchanged.

The tangential velocity is shown is part "b". This component of velocity does not have a great dependency on the axial direction. For this reason, it remains similar to the case where the injection took place at the endwall, as shown in Figure 4-5a.

It can be seen in Figure 4-10c that the radial velocity at the headwall is approximately zero. It increases as the fluid moves away from the inlet, reaching a maximum at the endwall, where most of the fluid is transferred from the outer vortex to the inner one. This behavior constitutes the reverse of the endwall injection case presented in Figure 4-6b. This example helps to verify that the formulation is error-free and symmetrical with respect to the injection location. When U_0 and U_L are switched, one arrives at the same outcome except for the axial direction of the flow. The same solution is hence reproduced irrespective of whether a profile is injected at the top or the bottom of the domain.

4.7.2 Infinitely Long Chamber

An infinite chamber can be simulated by equating the same axial velocity at both the endwall and the headwall. This setup eliminates the presence of a wall, specifically

one that reduces the axial velocity while the fluid is approaching it. To illustrate this characteristic, a linear Beltramian profile is imposed simultaneously as U_L and U_0.

Figure 4-11a and b provide the resulting axial and tangential velocity distributions, respectively. The absence of a rigid wall in the axial direction causes the profiles to become identical at all axial stations. In this situation, the radial velocity vanishes. This is an expected outcome because in an infinitely long chamber, no fluid transport can occur from the outer to the inner vortex.

4.7.3 Limitations

The present solution hinges upon the existence of bidirectional, cyclonic motion. As such, it cannot simulate a unidirectional flowfield for which only injection or suction profiles are established along an entire cross-section, be it the endwall or the headwall. For example, if an arbitrary velocity is imposed at the headwall that only involves fluid addition into the chamber (e.g., a fuel injection simulation), the solution emerging from

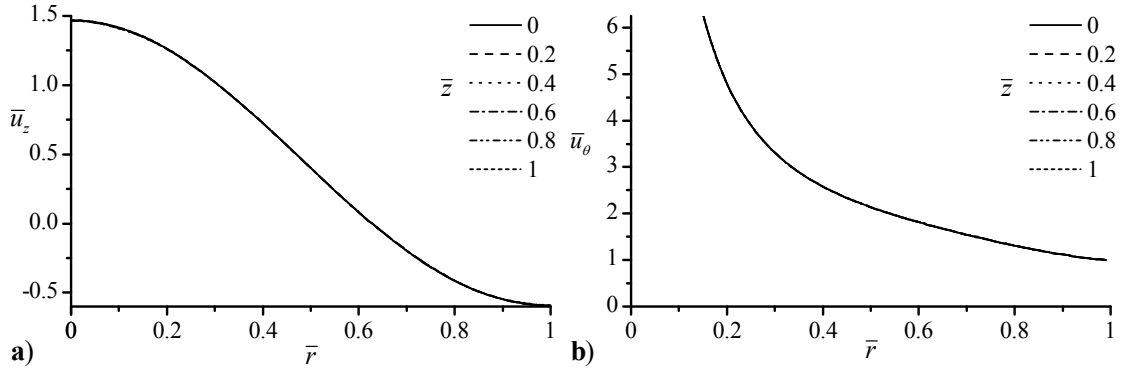

Figure 4-11. Radial distribution of a) axial and b) tangential velocities in a chamber of infinite length.

our framework will have a different profile at the same location; the intrinsically morphed velocity will be one that satisfies conservation of mass at that cross-section, notwithstanding the possible existence of another open boundary. The solution will hence exhibit a different profile from the one initially imposed, and the new profile will have both inflow and outflow segments that cancel each other out when integrated over the cross-section in question. Similar behavior occurs at the endwall.

As a demonstration to that case, an injection profile is imposed at the headwall using a polynomial function

$$\bar{U}_0(\bar{r}) = 0.1(1-\bar{r}^2) \tag{4.2}$$

At the headwall, a linear Beltramian profile is introduced with $\kappa = 0.125$ and $l = 1$.

$$\bar{U}_l(\bar{r}) = 1.47 J_0(\lambda_0 \bar{r}) + 0.05 \tag{4.3}$$

A constant of 0.05 is added to compansate for the additional fluid being injected at the headwall, such that both profiles satisfy the conservation of mass given by

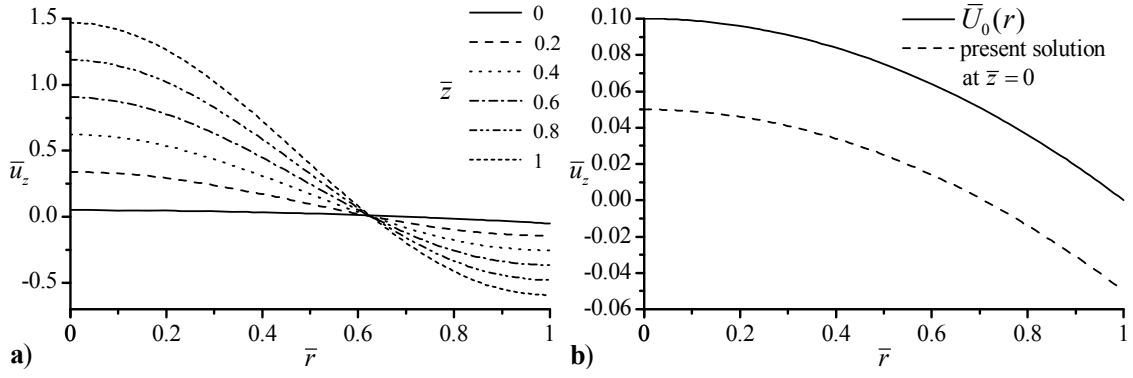

Figure 4-12. Axial velocity distribution versus the radial direction a) at different axial positions b) at the headwall with the boundary profile imposed.

$$\int_0^1 2\pi r\left[\bar{U}_l(\bar{r}) - \bar{U}_0(\bar{r})\right]\mathrm{d}r \tag{4.4}$$

Figure 4-12a shows the axial velocity distribution at different axial directions. At the endwall, the profile shifts by a value of 0.05 to match a profile that satisfies the conservation of mass with no regards to the headwall boundary. At $\bar{z} = 0$, a profile, similar in shape to the polynomial imposed, is returned by the solution. It has shifted downwards in such a way to satisfy conservation of mass at that boundary as shown in Figure 4-12b.

Concerning the radial velocity, only minor changes are detected at the headwall where the maximum radial velocity shifts slightly towards the core. The results are plotted in Figure 4-13a. The tangential velocities are presented in Figure 4-13b. It shows no notable changes compared to the "closed headwall" case. In order to connect the two boundaries such that mass injected at one end can be extracted at the other, a new analysis is required, and this will be addressed in future work.

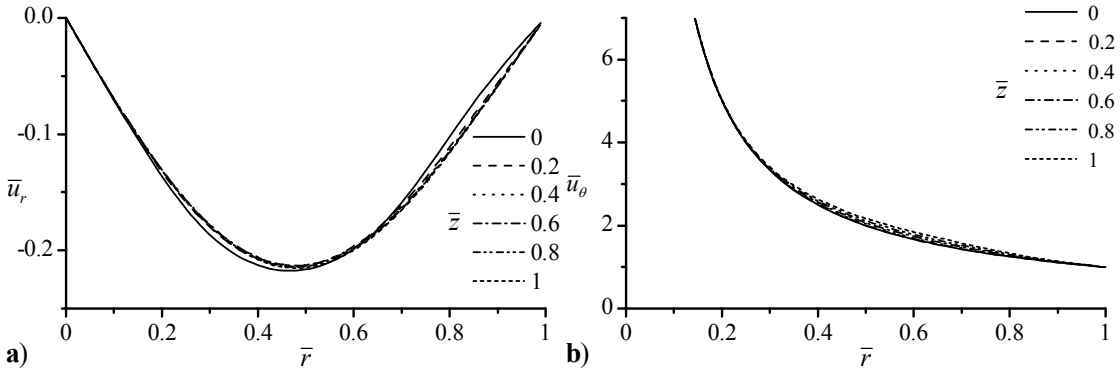

Figure 4-13. Radial distribution of the a) radial and b) axial velocity profiles at different axial positions.

Chapter 5

Core Viscous Correction

5.1 Problem Definition

The last term in Eq. (3.34) leads to a singularity at the centerline when $D \neq 0$. This is due to the inviscid assumption. In the previous section, two models of the Trkalian family were introduced. These models retain a zero tangential velocity at their core. Such models, although they satisfy the equations of motion, require further consideration for practical applications. Physically, there is no mechanism in the flow to produce such behavior because the models are inviscid, and viscosity is known to be a fluid property that prevents the singularity from occurring at the centerline. In the vicinity of the core, viscous stresses will dominate over the momentum forces. As a consequence the tangential velocity reduces from infinity, in inviscid flows, to zero in viscous flows. The free vortex-like behavior persists in the outer region for the Complex-Lamellar, linear and nonlinear Beltramian models.

To account for the viscous stresses in the equation, the viscous term in the tangential momentum equation must be retained. As shown by Majdalani and Chiaverini [36], one can begin by considering the regularized form of the tangential momentum equation,

$$\overline{u}_z \frac{\partial \overline{u}_\theta}{\partial \overline{z}} + \overline{u}_r \frac{\partial \overline{u}_\theta}{\partial \overline{r}} + \frac{\overline{u}_\theta \overline{u}_r}{\overline{r}} = \frac{1}{\mathrm{Re}}\left[\frac{\partial}{\partial \overline{r}}\left(\frac{1}{\overline{r}} \frac{\partial \left(\overline{r} \overline{u}_\theta \right)}{\partial \overline{r}} \right) + \frac{\partial^2 \overline{u}_\theta}{\partial \overline{z}^2} \right] \tag{5.1}$$

By solving Eq. (5.1) for the region close to the centerline, the result can be combined with the outer inviscid solution to produce a uniformly valid approximation over the domain extending from the centerline up to and excluding the sidewall.

Here the Reynolds number is based on the tangential reference velocity U and chamber radius a used for the normalization process in Section 3.4.

$$\mathrm{Re} = \frac{\rho U a}{\mu} \tag{5.2}$$

5.2 Viscous Solution

For practical applications in vortex driven engines, the Reynolds number is of order greater than 10^3. We define the perturbation parameter ε as

$$\varepsilon = \frac{1}{\mathrm{Re}} \tag{5.3}$$

In Section 4.3, it was shown that the models with singularity at the core have weak dependence on the axial position. The only slight variations that are observed belong to the Beltramian models. These variations are in the domain outside the core region of interest. Therefore, it is valid to assume

$$\frac{\partial \overline{u}_\theta}{\partial \overline{z}} = 0 \tag{5.4}$$

Based on Eqs. (5.3) and (5.4), Eq. (5.1) reduces to

$$\varepsilon \frac{\mathrm{d}}{\mathrm{d}\overline{r}}\left(\frac{1}{\overline{r}}\frac{d\overline{B}}{d\overline{r}}\right) - \frac{\overline{u}_r}{\overline{r}}\frac{\mathrm{d}\overline{B}}{\mathrm{d}\overline{r}} = 0 \tag{5.5}$$

where

$$\overline{B} = \overline{r}\overline{u}_\theta \tag{5.6}$$

To capture the behavior near the core, one must stretch the region near the axis of the chamber. This can be accomplished through the following transformation

$$\overline{s} = \frac{\overline{r}}{\delta(\varepsilon)} \tag{5.7}$$

The Bessel function embedded in the radial velocity term can be expanded using a Taylor series of the form

$$J_1(\lambda_n \delta \overline{s}) = \frac{\overline{s}\lambda_n}{2}\delta - \frac{\overline{s}^3\lambda_n^3}{16}\delta^3 + \ldots \tag{5.8}$$

Substituting back into Eq. (5.5), further simplifications lead to

$$\frac{\varepsilon}{\delta^2}\frac{\mathrm{d}^2\overline{B}}{\mathrm{d}\overline{s}^2} + \frac{\overline{s}}{2}K\frac{\mathrm{d}\overline{B}}{\mathrm{d}\overline{s}} - \frac{\varepsilon}{\delta^2\overline{s}}\frac{\mathrm{d}\overline{B}}{\mathrm{d}\overline{s}} = 0 \tag{5.9}$$

where

$$K = \sum_{n=0}^{k}\left[\frac{\overline{I}_l - \cos\left(\overline{\upsilon}_n l\right)\overline{I}_0}{\lambda_n J_0^2\left(\lambda_n\right)\sin\left(\overline{\upsilon}_n l\right)}\overline{\upsilon}_n\cos\left(\overline{\upsilon}_n\overline{z}\right) - \frac{\overline{I}_0}{\lambda_n J_0^2\left(\lambda_n\right)}\overline{\upsilon}_n\sin\left(\overline{\upsilon}_n\overline{z}\right)\right]\lambda_n$$

$$+\sum_{n=k+1}^{\infty}\left[\frac{\overline{I}_l - \cosh\left(\overline{\upsilon}_n^* l\right)\overline{I}_0}{\lambda_n J_0^2\left(\lambda_n\right)\sinh\left(\overline{\upsilon}_n^* l\right)}\overline{\upsilon}_n^*\cosh\left(\overline{\upsilon}_n^*\overline{z}\right) + \frac{\overline{I}_0}{\lambda_n J_0^2\left(\lambda_n\right)}\overline{\upsilon}_n^*\sinh\left(\overline{\upsilon}_n^*\overline{z}\right)\right]\lambda_n \tag{5.10}$$

A proper scaling can then be chosen such that $\varepsilon / \delta^2 = O(1)$; the distinguished limit becomes

$$\delta(\varepsilon) \approx \sqrt{\varepsilon} \tag{5.11}$$

The terms of order higher than $O(1)$ are immaterial, therefore can be removed. The differential equation to solve reduces to

$$\frac{\mathrm{d}^2 \overline{B}}{\mathrm{d}\overline{s}^2} + \frac{\overline{s}}{2} K \frac{\mathrm{d}\overline{B}}{\mathrm{d}\overline{s}} - \frac{1}{\overline{s}} \frac{\mathrm{d}\overline{B}}{\mathrm{d}\overline{s}} = 0 \tag{5.12}$$

for which a solution may be expressed as:

$$\overline{B}^{(i)} = \frac{C_1}{K} e^{-\frac{K}{4}\overline{s}^2} + C_2 \tag{5.13}$$

The two constants C_1 and C_2 must be determined form the physical requirements as it will be shown next.

5.3 Boundary Conditions and Asymptotic Matching

The first boundary condition consists of requiring the tangential velocity to vanish at the core. This implies that

$$\overline{u}_\theta(0) = 0 \Rightarrow \overline{B}(0) = 0 \Rightarrow \frac{C_1}{K} + C_2 = 0 \tag{5.14}$$

Prandtl's Matching Principle can then be applied in order to match the inner approximation to the outer inviscid solution given earlier by Eq. (3.34). We write:

$$\lim_{\overline{s}\to\infty} \overline{u}_\theta^{(i)} = \lim_{\overline{r}\to 0} \overline{u}_\theta^{(o)} = \overline{u}_\theta^{(cl)} \tag{5.15}$$

where $\overline{u}_\theta^{(cl)}$ represents the common limit.

From Eqs. (5.14) and (5.15), the two constants C_1 and C_2 may be fully determined. The final inner solution becomes

$$\overline{u}_\theta^{(i)} = -\frac{\sqrt{\overline{D}}}{\overline{r}} e^{-\frac{K}{4}\mathrm{Re}\overline{r}^2} + \frac{\sqrt{\overline{D}}}{\overline{r}} \tag{5.16}$$

To get a solution that is uniformly valid over the entire domain excluding the walls, the inner and outer solutions can be combined to form what is known as the composite solution,

$$\overline{u}_\theta^{(c)} = \overline{u}_\theta^{(i)} + \overline{u}_\theta^{(o)} - \overline{u}_\theta^{(cl)} \tag{5.17}$$

$$\overline{u}_\theta^{(c)} = \left(\overline{C}^2 \left\{ \sum_{n=0}^{k} \left[\frac{\overline{I}_l - \cos\left(\overline{\upsilon}_n l\right)\overline{I}_0}{\lambda_n J_0^2\left(\lambda_n\right)\sin\left(\overline{\upsilon}_n l\right)} \sin\left(\overline{\upsilon}_n \overline{z}\right) + \frac{\overline{I}_0 \cos\left(\overline{\upsilon}_n \overline{z}\right)}{\lambda_n J_0^2\left(\lambda_n\right)} \right] J_1\left(\lambda_n \overline{r}\right) \right.$$

$$\left. + \sum_{n=k+1}^{\infty} \left[\frac{\overline{I}_l - \cosh\left(\overline{\upsilon}_n^* l\right)\overline{I}_0}{\lambda_n J_0^2\left(\lambda_n\right)\sinh\left(\overline{\upsilon}_n^* l\right)} \sinh\left(\overline{\upsilon}_n^* \overline{z}\right) + \frac{\overline{I}_0 \cosh\left(\overline{\upsilon}_n^* \overline{z}\right)}{\lambda_n J_0^2\left(\lambda_n\right)} \right] J_1\left(\lambda_n \overline{r}\right) \right\}^2 + \frac{\overline{D}}{\overline{r}^2} \Bigg)^{\frac{1}{2}} - \frac{\sqrt{\overline{D}}}{\overline{r}} e^{-\frac{K}{4}\mathrm{Re}\overline{r}^2}$$

(5.18)

Equation (5.18) is the final solution emerging from this analysis. It is no longer singular at the centerline, but rather uniformly valid for $0 \le \overline{r} < 1$. It should be noted that the last term incorporates the effects of viscous attenuation near the core. As depicted by the solution, these depend mainly on the product of the Reynolds number and the term K; the latter incorporates the source integrals $\overline{I}_0$ and $\overline{I}_l$ as well as the aspect ratio of the chamber. At the outset, the viscous corrections will change with different boundary conditions.

The grouping of $K\,\mathrm{Re}$ plays the role of the vortex Reynolds number V reported by Majdalani and Chiaverini [36] and written as

$$V = \frac{\mathrm{Re}}{\sigma l} \tag{5.19}$$

It thus combines the effects of the Reynolds number, swirl number, and chamber aspect ratio. In the present generalization, the swirl number is imbedded within the boundary conditions and does not appear explicitly. Here too, K is a function of the chamber aspect ratio. The effects of these parameters will be further discussed in the next chapter.

It is noted that as $\mathrm{Re} \to \infty$, $\overline{u}_\theta^{(c)} \to \overline{u}_\theta^{(o)}$. The outer solution is restored. Conversely, as $\overline{r} \to 0$, correlated with a finite Reynolds number, Eq. (5.18) can be expanded to

$$\overline{u}_\theta^{(c)} = \frac{\sqrt{\overline{D}}}{\overline{r}}\left(1 - e^{-\frac{K}{4}\mathrm{Re}\,\overline{r}^2}\right) = \frac{\sqrt{\overline{D}}}{4} K\,\mathrm{Re}\,\overline{r} + O(\overline{r}^3) \tag{5.20}$$

Eq. (5.20) can be related to the forced vortex relation given by $\overline{u}_\theta^{(c)} \sim \omega_f \overline{r}$ where ω_f is the angular velocity of the core given by

$$\omega_f = \frac{\sqrt{\overline{D}}}{4} K\,\mathrm{Re} \tag{5.21}$$

5.4 Vorticity Correction

Now that viscosity is introduced to the system, additional vorticity is generated inside the chamber. Using the same formulations as in Section 3.5, new vorticity equations may be derived. One gets

$$\bar{\omega}_r^{(c)} = -\frac{\bar{C}^2}{\bar{r}\sqrt{\bar{C}^2\bar{\psi}^2 + \bar{D}}}\bar{\psi}\frac{\partial\bar{\psi}}{\partial\bar{z}} - \sqrt{\bar{D}}\frac{\mathrm{d}K}{\mathrm{d}\bar{z}}\frac{\mathrm{Re}\,\bar{r}}{4}e^{\frac{-K}{4}\mathrm{Re}\bar{r}^2} \tag{5.22}$$

where

$$\frac{\mathrm{d}K}{\mathrm{d}\bar{z}} = -\sum_{n=0}^{k}\left[\frac{\bar{I}_l - \cos(\bar{\upsilon}_n l)\bar{I}_0}{\lambda_n J_0^2(\lambda_n)\sin(\bar{\upsilon}_n l)}\bar{\upsilon}_n{}^2\sin(\bar{\upsilon}_n\bar{z}) + \frac{\bar{I}_0}{\lambda_n J_0^2(\lambda_n)}\bar{\upsilon}_n{}^2\cos(\bar{\upsilon}_n\bar{z})\right]\lambda_n$$

$$+\sum_{n=k+1}^{\infty}\left[\frac{\bar{I}_l - \cosh(\bar{\upsilon}_n^* l)\bar{I}_0}{\lambda_n J_0^2(\lambda_n)\sinh(\bar{\upsilon}_n^* l)}\bar{\upsilon}_n^{*2}\sinh(\bar{\upsilon}_n^*\bar{z}) + \frac{\bar{I}_0}{\lambda_n J_0^2(\lambda_n)}\bar{\upsilon}_n^{*2}\cosh(\bar{\upsilon}_n^*\bar{z})\right]\lambda_n \tag{5.23}$$

The tangential component of the vorticity is unaffected by the tangential viscous core correction because it is independent of the tangential velocity. It only depends on u_r and u_θ as expressed by Eq. (3.39).

Concerning the axial component of vorticity, it can be presented as

$$\bar{\omega}_z^{(c)} = \frac{\bar{C}^2}{\bar{r}\sqrt{\bar{C}^2\bar{\psi}^2 + \bar{D}}}\bar{\psi}\frac{\partial\bar{\psi}}{\partial\bar{r}} + \frac{1}{2}\sqrt{\bar{D}}K\,\mathrm{Re}\,e^{-\frac{K}{4}\mathrm{Re}\bar{r}^2} \tag{5.24}$$

and the total vorticity by

$$\bar{\omega}^{(c)} = \sqrt{\left[\omega_r^{(c)}\right]^2 + \omega_\theta^2 + \left[\omega_z^{(c)}\right]^2} \tag{5.25}$$

The evalutaion of $\bar{\omega}^{(c)}$ may be relegated to a symbolic program and is omitted here for brevity.

5.5 Pressure Correction

In Chapter 4, it was shown that the pressure of the Complex-Lamellar, linear and nonlinear Beltramians boundary condition generate a singularity at the centerline. From the Euler momentum equations, it can be seen that the pressure gradient in the radial

direction is dependent on the tangential velocity, the source of the singularity. The viscous rectification of $\overline{u}_\theta$ near the core also leads to the removal of the ensuing pressure distribution, as it will be demonstrated later. The corrected pressure may be extracted from:

$$-\frac{\partial \overline{p}^{(c)}}{\partial \overline{r}} = \overline{u}_z \frac{\partial \overline{u}_r}{\partial \overline{z}} + \overline{u}_r \frac{\partial \overline{u}_r}{\partial \overline{r}} - \frac{\left[\overline{u}_\theta^{(c)}\right]^2}{\overline{r}} \tag{5.26}$$

The axial and radial velocities used in Eq. (5.26) are the inviscid solutions given by Eqs. (3.32) and (3.33), respectively. These are still valid because no boundary layer exists in these directions near the centerline.

Chapter 6

Characterization of the Core Viscous Correction

The introduction of viscosity in the tangential momentum has substantial bearing on the swirl velocity, vorticity distribution, and pressure. These features are examined in this chapter.

6.1 Tangential Velocity

The swirl velocity distribution is given by Eq. (3.34). The last term on the right hand side represents the viscous correction. It is dependent on the Reynolds number given by Eq. (5.2). Figure 6-1 shows the variation of the tangential velocity at different axial positions. The velocity at the sidewall matches the injection velocity $U_\theta(r)$. The velocity then increases as it approaches the core region until it reaches a maximum $\overline{u}_{\theta\max}^{(c)}$. This point bounds the region inside of which viscous forces dominate. After peaking at $\overline{r} = \overline{r}_{\max}$, the swirl velocity diminishes until it reaches zero at the centerline.

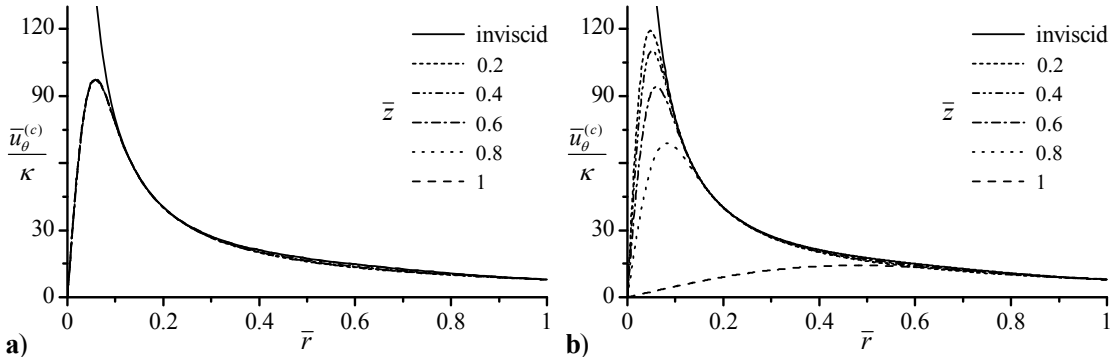

Figure 6-1. Tangential velocity plots versus the radial direction for different axial positions using a) linear and b) nonlinear Beltramian boundary conditions. Here l = 1, κ = 0.125 and Re = 1000.

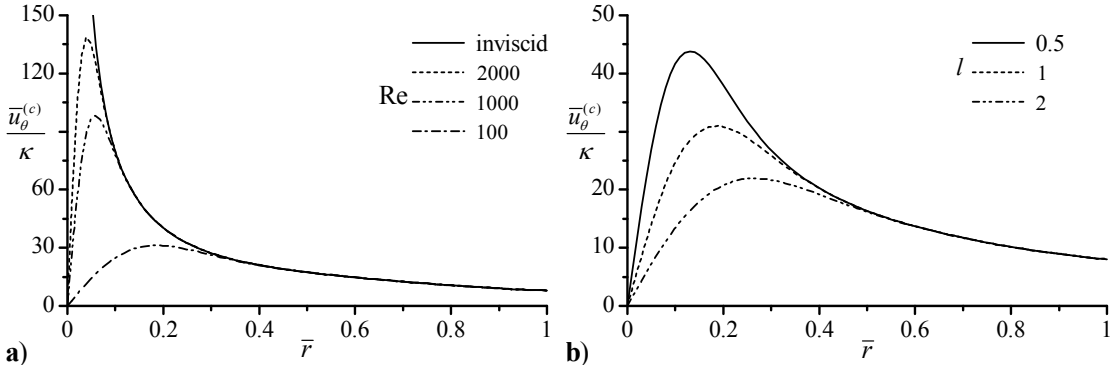

Figure 6-2. Tangential velocity plots versus the radial direction for different a) Reynolds number and b) aspect ratios. Results correspond to the linear Beltramian case with κ = 0.125, l = 1, $\overline{z} = 0.5l$ and Re = 100 where needed.

Figure 6-1a and b depict the tangential velocity variations at different axial positions for two different sets of boundary conditions: the linear and nonlinear Beltramian velocity distributions [13]. The linear Beltramian boundary condition has a swirl momentum constant $\overline{C}$ of 3.828, whereas, in the Nonlinear Beltramian case, $\overline{C} = 4.137$. The term in Eq. (5.18) that is responsible for the axial dependency is $\overline{\upsilon}_n \cos \overline{\upsilon}_n \overline{z}$; it is embedded in K. Equation (3.9) shows that $\overline{\upsilon}$ diminishes as $\overline{C}$ approaches the eigenvalues λ_n. Since most of the weight in the summation series comes from the first term, it is sufficient for $\overline{C}$ to approach the first zero of the Bessel function of the first kind $(\lambda_1 = 3.832)$ to eliminate the dependency of the core tangential velocity on the axial position. This behavior is exhibited by the linear Beltramian injection case, as shown in in Figure 6-1a. As for the nonlinear Beltramian inlet velocity, it may be seen in Figure 6-1b that viscous effects are increased as the flow approaches the headwall.

Figure 6-2a shows the variation of $\overline{u}_\theta^{(c)}$ for different Reynolds numbers. As Re increases, the core area decreases. For low swirl intensities, the viscous effects cover a wider zone of the chamber. The radius of the core can be obtained by calculating the radial position at which $\overline{u}_{\theta \max}^{(c)}$ occurs. Unfortunately, no exact solution for $\overline{r}_{\max}$ can be extracted. Root finding techniques are used for this purpose. Table 6-1 quantifies the radius of the viscous core as predicted by the Complex-Lamellar viscous correction [36] and the present solution, with boundary conditions pertaining to the Complex-Lamellar (CL), linear Beltramian (LB) and nonlinear Beltramian (NB), for several values of Re.

Further analysis of Eq. (5.18) also reveals a relation between the chamber aspect ratio and the size of the viscous region. Figure 6-2b displays three plots of the tangential velocity over the radial direction for 3 different aspect ratios. As l increases, the role of viscosity is magnified. This result confirms the study by Majdalani and Chiaverini [36].

6.2 Vorticity Correction

Figure 6-3 describes the vorticity distribution in the vortex chamber with and

Table 6-1. Radial thickness of the viscous core for $\kappa = 0.125$ and $l = 1$

	$\overline{r}_{max}$			
Re	**CL[a] [36], $\forall \bar{z}$**	**CL[b], $\bar{z} = 0.5l$**	**LB[b], $\forall \bar{z}$**	**NB[b], $\bar{z} = 0.5l$**
2000	0.057	0.064	0.041	0.039
1500	0.065	0.074	0.048	0.045
1200	0.073	0.082	0.053	0.051
1000	0.080	0.090	0.058	0.056
500	0.113	0.128	0.083	0.079
200	0.179	0.202	0.131	0.124
100	0.253	0.286	0.186	0.176
50	0.358	0.404	0.264	0.252

[a] Original model

[b] Present solution with the referenced model used as boundary condition

without viscosity. Parts “a”, “b” and “c” include viscosity in the core region and Part “d” corresponds to the inviscid model described in Chapter 4. Interestingly, we find that the vorticity generated in the viscous core visibly exceeds the one introduced into the chamber at the boundary by the incoming fluid that possesses a swirling component in its inlet plane. Even for a very low Reynolds number of, say, 100, the magnitude of the vorticity at the core will be approximately ten times larger than the one introduced into the chamber by virtue of the velocity imposed at the boundary.

As the Reynolds number decreases, the area where vorticity is generated expands, but the magnitude of the vorticity per unit volume decreases. It is also noted that the vorticity is confined to the core region and does not spread to the outer parts of the chamber. This is mainly due to the fact that at the core, the fluid directly travels towards the endwall and exits the chamber.

It should be also noted that as the Reynolds number approaches infinity, the momentum forces dominate over the entire domain. Viscous effects will be negligible. From a mathematical point of view, as $\mathrm{Re} \to \infty$, Eqs. (5.22), (5.24) and (5.25) reduce to their inviscid counterparts given by Eqs. (3.37), (3.40) and (3.42), respectively.

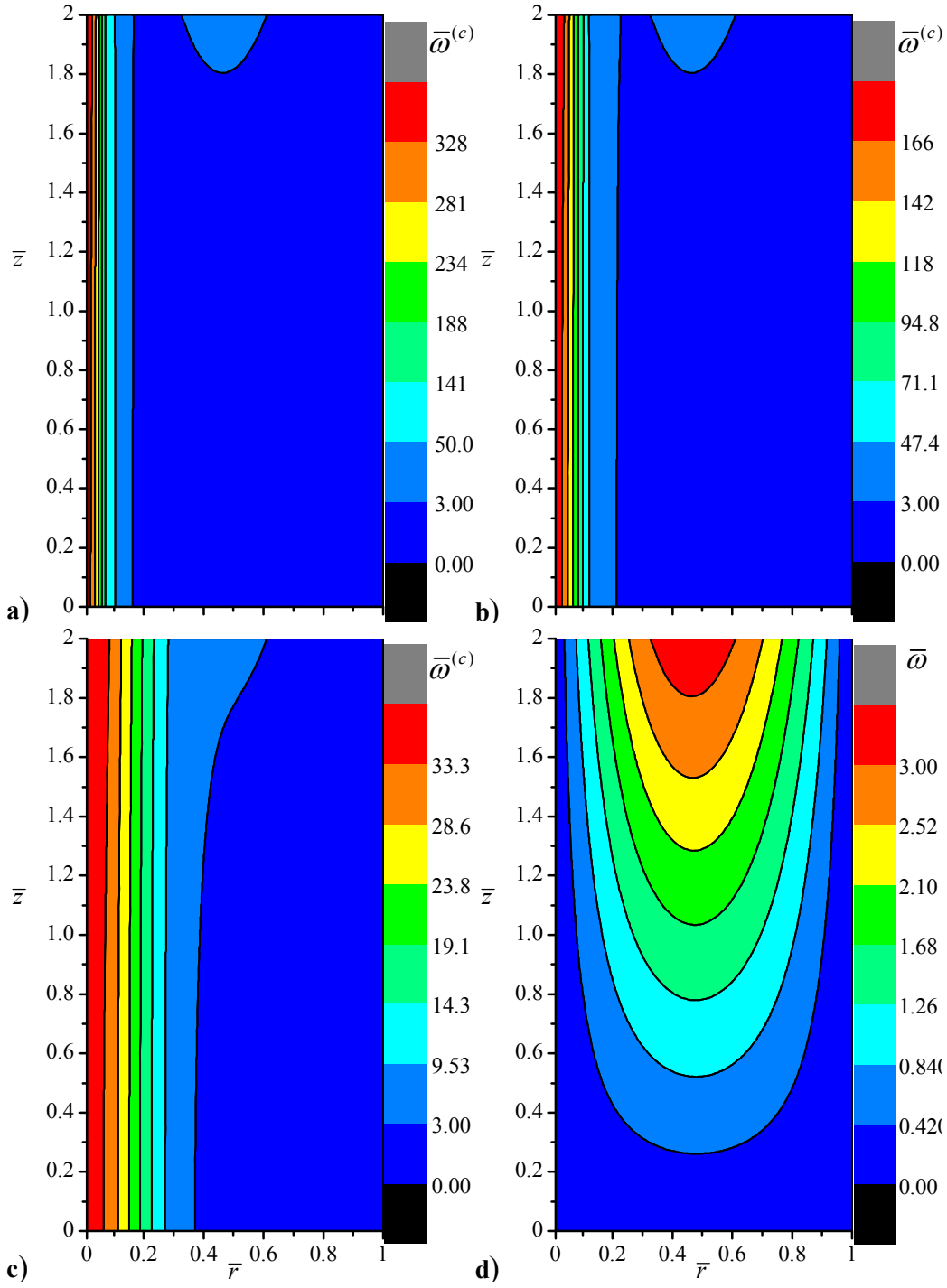

Figure 6-3. Vorticity distribution in a chamber for a) Re = 1000, b) Re = 500, c) Re = 100 and d) inviscid flows. Results correspond to the linear Beltramian case with l = 2 and κ = 0.125.

6.3 Pressure Correction

The pressure gradient in the radial direction increases when moving away from the sidewall toward the centerline. In the inviscid case, a singularity is detected that causes the total pressure to reach vacuum at the centerline as it can be seen in Figure 4-8 for the Complex-Lamellar, linear and nonlinear Beltramians. Figure 6-4 shows the role of viscosity in reducing the pressure gradient near the core until it vanishes at $\bar{r} = 0$.

Figure 6-5 displays the variation of the total pressure in the vicinity of the core. The pressure decreases as it approaches the center of the chamber, reaching a minimum at $\bar{r} = 0$. The Reynolds number appears to have a substantial impact on the variation of the pressure. The higher the Reynolds number is, the greater the difference between the sidewall and core pressure. At radial positions greater than 0.15, all pressure profiles converge to the same value as the inviscid solution.

The cases shown in Figure 6-4 and Figure 6-5 are for the linear Beltramian profile with a chamber aspect ratio of 1. Similar viscous core correction corrections can be applied to the Complex-Lamellar and the nonlinear Beltramian profiles.

So far no exact analytical solution for the total pressure can be derived due to the presence of integrals that still do not yield a closed form solution. In this study, series approximations are used to solve for the integrals and generate the plots.

6.4 Remarks

This chapter has focused on the core boundary layer that is generated by introducing viscosity to the system. This boundary layer only affects the velocity in the

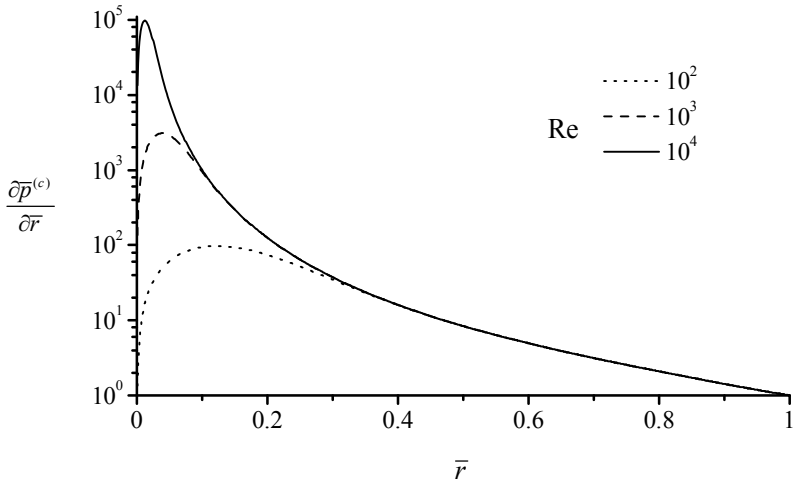

Figure 6-4. Radial variation of the pressure gradient at different Reynolds numbers.

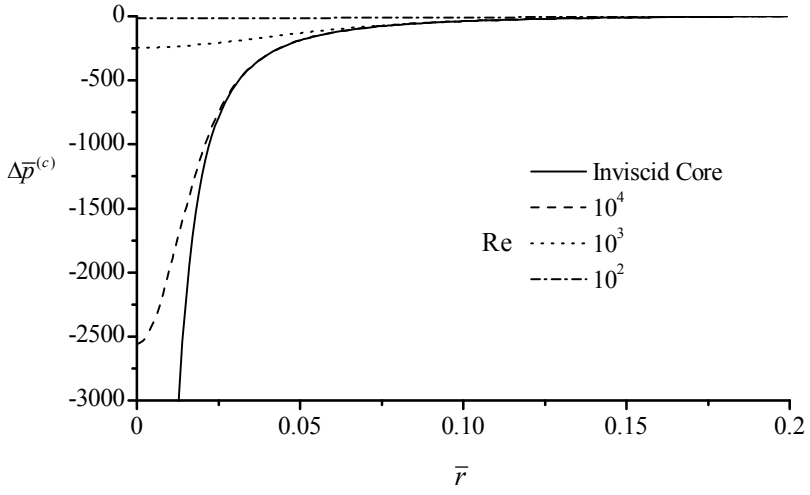

Figure 6-5. Pressure variation near the core of the combustion chamber for the inviscid and viscous cases.

tangential direction and has no impact on the axial and radial velocities near the centerline.

Viscosity also creates other boundary layers at the sidewall and headwall of the combustion chamber. These give rise to no slip conditions for all components of velocity. Although friction significantly reduces the velocities near the walls, its impact remains limited to a narrow region. The sidewall and headwall boundary layers are important for computing the shear stresses exerted on the walls that clearly affect many calculations, such as those concerned with stability, torques, losses, the friction coefficient, etc. These along other flow features will be addressed in future work.

Chapter 7

Conclusions

An exact Eulerian solution for the axisymmetric bidirectional vortex is derived in this study. The new solution is general enough to cope with arbitrary boundary conditions for the axial and tangential velocities. The axial velocities at the boundaries affect the source terms I_0 and I_L in Eq. (3.16), which, in turn, controls the fluctuations of the velocities in all directions. For the azimuthal direction, two terms are identified that help to define the tangential velocity at the boundary. The first is the tangential surface parameter, D, that sets the tangential velocity at the sidewall and only affects the azimuthal velocity in the rest of the domain. Nonetheless, the axial and radial velocities remain independent of D. The second parameter C is dubbed the swirl momentum constant; it is used to prescribe the distribution of the tangential velocity in the radial direction, therefore, setting the amount of vorticity introduced into the domain. This parameter is shown to affect the distribution of the velocity in all directions, as well as controlling the penetration depth of rotationality into the chamber.

To demonstrate the generality of the solution, five former solutions were regenerated using the same boundary conditions as the original models. Only some discrepancies were detected when generating the axial and radial velocities of the Complex-Lamellar model due to its roots being from a different formulation and fundamental assumption.

The axial velocity displays the tendency to reproduce the same profiles imposed at the endwalls although its shapes may often shift in the axial direction as the flow changes from its basic configuration to the one prescribed at its boundary. In all of the cases tested, the magnitude of the axial speed is seen to decrease until it vanishes at the headwall. This behavior is consistent with the measurements obtained in two experiments by Smith [26, 27].

The change in the radial velocity with the radius is consistent in all the cases studied. It is zero at the core and the sidewall and reaches a maximum near the centerline. The location of the maximum radial velocity varies with the boundary condition. The change of the radial velocity in the axial direction is dependent on the capability of the rotational particles to penetrate deep into the chamber. This is also controlled by the boundary condition, specifically the swirl momentum constant C as stated earlier. It is also shown that the boundary conditions pertaining to the nonlinear Beltramian model produce the least amount of flow leakage from the outer vortex into the inner vortex, especially near the endwall. This feature is important in vortex rocket engines because it increases the engine's efficiency by minimizing the amount of oxidizer loss.

The swirl velocity is set at the sidewall by the tangential surface parameter D. It increases as we approach the core to the extent of reaching infinity at the centerline, except for the Trkalian cases which were shown to be only academic solutions that do not represent real flows. This component of velocity shows very slight dependence on the axial position.

Concerning the pressure distribution, it is shown that the highest pressure concentration exists at the corner joining the sidewall and headwall. The closer the location is to the nozzle, the lower the pressure will be. In the radial direction, the pressure increases going from the centerline to the sidewall, as one would expect given centrifugal action.

In Chapter 5, a viscosity correction is added to the inviscid solution near the centerline. The viscous solution removes the singularities for the tangential velocity and pressure. The tangential velocity increases as it approaches the centerline, until it reaches a maximum, where viscous forces dominate, and the swirl velocity is reduced till it reaches zero at $\bar{r} = 0$. This component of velocity shows no dependency on the axial position in the core region if the swirl momentum constant falls within the neighborhood of the first root of the Bessel function of the first kind; else, viscous effects are reduced as the fluid approaches the headwall.

The pressure behaves the same as the inviscid solution in the outer region. It decreases as we move away from the sidewall. Instead of reaching a vacuum at the centerline (cf. the inviscid solution), the pressure gradient decreases when viscous effects begin to dominate. The total pressure reaches a finite minimum at the centerline. The

low pressure near the centerline may be viewed as the driving force that causes the outer vortex to spiral toward the headwall, instead of spilling directly out of the nozzle/discharge port. An increase in Re will hence give rise to an increase in chamber pressure.

The viscous correction leads to the generation of vorticity within the core region. It is shown that the vorticity produced in the vortex chamber by viscosity exceeds the vorticity that may be introduced through the inlet plane by the flow injection boundary condition. As the Reynolds number decreases, vorticity is generated in a larger portion of the chamber around the core; however, it remains confined to that region until exiting because of the axial velocity in the core region which continuously travels toward the endwall. Evidently, as $\mathrm{Re} \to \infty$, the inviscid solution is retrieved.

The aspect ratio of the chamber turns out to be an effective parameter to consider. As l increases, the viscous core region increases in diameter, thus leading to a wider spread of viscous effects.

7.1 Future Work

A cold flow experiment and/or numerical analysis should be performed. This will allow one to verify the accuracy of the findings presented in this work.

As an extension to this investigation, a viscous correction at the walls should be explored. The resulting analysis would elucidate the wall boundary layer effects on bidirectional vortex development.

An extension of the present framework would be very informative, especially one that would encompass a wider range of boundary conditions. These may include a headwall velocity profile that can properly simulate fuel injection in rocket engines or particle extraction in industrial cyclones. Further exploration of the present equations may also reveal a potential to mimic vortices with multiple mantles.

References

References

1. Sutton, G.P. and O. Biblarz, *Rocket Propulsion Elements*2001, New York: John Wiley.
2. Chiaverini, M.J., et al. *Fuel decomposition and boundary-layer combustion processes of hybrid rocket motors*. 1995. San Diego, CA.
3. Kuo, K. and M.J. Chiaverini, *Challenges of Hybrid Rocket Propulsion in the 21st Century*, in *Fundamentals of Hybrid Rocket Combustion and Propulsion*, K. Kuo and M.J. Chiaverini, Editors. 2007, AIAA Progress in Astronautics and Aeronautics: Washington, DC. p. 591-636.
4. Chiaverini, M.J., et al. *Vortex combustion chamber development for future liquid rocket engine applications*. in *AIAA*. 2002. Indianapolis, IN.
5. Penner, S.S., *Elementary considerations of the fluid mechanics of tornadoes and hurricanes.* Acta Astronautica, 1972. **17**: p. 351-362.
6. Königl, A., *Stellar and galactic jets: theoretical issues.* Canadian Journal of Physics, 1986. **64**: p. 362-368.
7. Kirshner, R.P., *The Extravagant Universe: Exploding Stars, Dark Energy, and the Accelerating Cosmos*2004, Princeton, New Jersey: Princeton University Press.
8. Reydon, R.F. and W.H. Gauvin, *Theoretical and experimental studies of confined vortex flow.* The Canadian Journal of Chemical Engineering, 1981. **59**: p. 14-23.

9. Gloyer, P.W., W.H. Knuth, and J. Goodman. *Overview of initial research into the effects of strong vortex flow on hybrid rocket combustion and performance*. in *CSTAR Fifth Annual Symposium*. 1993. Tullahoma, TN.

10. Knuth, W.H., et al., *Gas-Fed, Vortex Injection Hybrid Rocket Engine*, 1996, NASA Marshall Space Flight Center: Huntsville, AL.

11. Chiaverini, M.J., et al. *Vortex thrust chamber testing and analysis for O2-H2 propulsion applications*. in *AIAA*. 2003. Huntsville, AL.

12. Matveev, I., S. Matveeva, and S. Serbin. *Design and preliminary test results of the plasma assisted tornado combustor*. in *AIAA*. 2007. Cincinnati, OH.

13. Majdalani, J. *Exact Eulerian solutions of the cylindrical bidirectional vortex*. in *AIAA*. 2009. Denver, CO.

14. Rankine, W.J.M., *A Manual of Applied Mechanics*. 9th ed1858, London, UK: C. Griffin and Co.

15. Lamb, H., *Hydrodynamics*. 6th ed1932, Cambridge, UK: Cambridge University Press.

16. Oseen, C.W., *Uber Wirbelbewegung in einer reibenden FlÃ¼ssigkeit. Ark. f.* Mat. Astron. Fys, 1912. **7**.

17. Burgers, J.M., *On the resistance of fluids and vortex motion.* Proceedings of Koninklijke Nederlandse Akademie van Wetenschappen (KNAW), 1921. **23**(1): p. 774-782.

18. Burgers, J.M., *A mathematical model illustrating the theory of turbulence.* Advances in Applied Mechanics, 1948. **1**: p. 171-199.

19. Rott, N., *Boundary layers and their interactions in rotating flows.* Progress in Aerospace Sciences, 1966. **7**: p. 111-144.

20. Rott, N., *On the viscous core of a line vortex.* Zeitschrift für Angewandte Mathematik und Physik (ZAMP), 1958. **9**(5): p. 543-553.

21. Sullivan, R.D., *A two-cell vortex solution of the Navier-Stokes equations.* Journal of the Aerospace Sciences, 1959. **26**: p. 767-768.

22. Bloor, M.I.G. and D.B. Ingham, *The flow in industrial cyclones.* Journal of Fluid Mechanics, 1987. **178**(1): p. 507-519.

23. Barber, T.A. and J. Majdalani. *Exact Eulerian solution of the conical bidirectional vortex*. in *AIAA*. 2009. Denver, CO.

24. Batterson, J.W., B.A. Maicke, and J. Majdalani. *Advancements in theoretical models of confined vortex fowfields*. in *JANNAF*. 2007. Denver, CO.

25. Kelsall, D.F., *A study of motion of solid particles in a hydraulic cyclone.* Transactions of the Institution of Chemical Engineers, 1952. **30**: p. 87-103.

26. Smith, J.L., *An experimental study of the vortex in the cyclone separator.* Journal of Basic Engineering-Transactions of the ASME, 1962. **84**(4): p. 602-608.

27. Smith, J.L., *An analysis of the vortex flow in the cyclone separator.* Journal of Basic Engineering-Transactions of the ASME, 1962. **84**(4): p. 609-618.

28. Hoekstra, A.J., J.J. Derksen, and H.E.A. Van den Akker, *An experimental and numerical study of turbulent swirling flow in gas cyclones.* Chemical Engineering Science, 1999. **54**(13): p. 2055-2065.

29. Derksen, J.J. and H.E.A. Van den Akker, *Simulation of vortex core precession in a reverse flow cyclone.* AIChE Journal, 2000. **46**(7): p. 1317-1331.

30. Fang, D., J. Majdalani, and M.J. Chiaverini. *Simulation of the cold-wall swirl driven combustion chamber*. in *AIAA*. 2003. Huntsville, AL.

31. Rom, C.J., M.H. Anderson, and M.J. Chiaverini. *Cold flow analysis of a vortex chamber engine for gelled propellant combustor applications*. in *AIAA*. 2004. Fort Lauderdale, FL.

32. Vyas, A.B. and J. Majdalani, *Exact solution of the bidirectional vortex.* AIAA Journal, 2006. **44**(10): p. 2208-2216.

33. Majdalani, J. and S.W. Rienstra, *On the bidirectional vortex and other similarity solutions in spherical coordinates.* Journal of Applied Mathematics and Physics (ZAMP), 2007. **58**(2): p. 289-308.

34. Majdalani, J. and A.B. Vyas. *Rotational axisymmetric mean flow for the vortex injection hybrid rocket engine*. in *AIAA*. 2004. Fort Lauderdale, FL.

35. Majdalani, J., *Vortex Injection Hybrid Rockets*, in *Fundamentals of Hybrid Rocket Combustion and Propulsion*, K. Kuo and M.J. Chiaverini, Editors. 2007, AIAA Progress in Astronautics and Aeronautics: Washington, DC. p. 247-276.

36. Majdalani, J. and M.J. Chiaverini, *On steady rotational cyclonic flows: The viscous bidirectional vortex.* Physics of Fluids, 2009. **21**(10): p. 103603-15.

37. Batterson, J.W. and J. Majdalani. *On the boundary layers of the bidirectional vortex*. in *AIAA*. 2007. Miami, FL.

38. Batterson, J.W. and J. Majdalani, *Sidewall boundary layers of the bidirectional vortex.* Journal of Propulsion and Power, 2010. **26**(1): p. 102-112.

39. Maicke, B.A. and J. Majdalani, *A constant shear stress core flow model of the bidirectional vortex.* Proceedings of the Royal Society of London, Series A, 2009. **465**(2103): p. 915-935.

40. Wolfram, S., *Mathematica. A System for Doing Mathematics on Computer.*, 1988, Addison Wesley: Reading, MA.

Appendix

Mean velocity flow field equations

Inviscid Axial velocity

$$u_z = \left\{ \begin{array}{l} \sum_{n=0}^{k} \left[\frac{I_L - \cos(\upsilon_n L) I_0}{\lambda_n a J_0^2(\lambda_n) \sin(\upsilon_n L)} \sin(\upsilon_n z) + \frac{I_0 \cos(\upsilon_n z)}{\lambda_n a J_0^2(\lambda_n)} \right] \frac{\lambda_n}{a} J_0\left(\frac{\lambda_n}{a} r\right) \\ + \sum_{n=k+1}^{\infty} \left[\frac{I_L - \cosh(\upsilon_n^* L) I_0}{\lambda_n a J_0^2(\lambda_n) \sinh(\upsilon_n^* L)} \sinh(\upsilon_n^* z) + \frac{I_0 \cosh(\upsilon_n^* z)}{\lambda_n a J_0^2(\lambda_n)} \right] \frac{\lambda_n}{a} J_0\left(\frac{\lambda_n}{a} r\right) \end{array} \right\}$$

Inviscid Radial Velocity

$$u_r = \left\{ \begin{array}{l} -\sum_{n=0}^{k} \left[\frac{I_L - \cos(\upsilon_n L) I_0}{\lambda_n a J_0^2(\lambda_n) \sin(\upsilon_n L)} \upsilon_n \cos(\upsilon_n z) - \frac{I_0 \upsilon_n \sin(\upsilon_n z)}{\lambda_n a J_0^2(\lambda_n)} \right] J_1\left(\frac{\lambda_n}{a} r\right) \\ -\sum_{n=k+1}^{\infty} \left[\frac{I_L - \cosh(\upsilon_n^* L) I_0}{\lambda_n a J_0^2(\lambda_n) \sinh(\upsilon_n^* L)} \upsilon_n^* \cosh(\upsilon_n^* z) + \frac{I_0 \upsilon_n^* \sinh(\upsilon_n^* z)}{\lambda_n a J_0^2(\lambda_n)} \right] J_1\left(\frac{\lambda_n}{a} r\right) \end{array} \right\}$$

Inviscid Tangential Velocity

$$u_\theta = \left(C^2 \left\{ \begin{array}{l} \sum_{n=0}^{k} \left[\frac{I_L - \cos(\upsilon_n L) I_0}{\lambda_n a J_0^2(\lambda_n) \sin(\upsilon_n L)} \sin(\upsilon_n z) + \frac{I_0 \cos(\upsilon_n z)}{\lambda_n a J_0^2(\lambda_n)} \right] J_1\left(\frac{\lambda_n}{a} r\right) \\ + \sum_{n=k+1}^{\infty} \left[\frac{I_L - \cosh(\upsilon_n^* L) I_0}{\lambda_n a J_0^2(\lambda_n) \sinh(\upsilon_n^* L)} \sinh(\upsilon_n^* z) + \frac{I_0 \cosh(\upsilon_n^* z)}{\lambda_n a J_0^2(\lambda_n)} \right] J_1\left(\frac{\lambda_n}{a} r\right) \end{array} \right\}^2 + \frac{D}{r^2} \right)^{\frac{1}{2}}$$

Viscous Core Tangential Velocity

$$\overline{u}_\theta^{(c)} = \left(\overline{C}^2 \left\{ \sum_{n=0}^{k} \left[\frac{\overline{I}_l - \cos(\overline{\upsilon}_n l) \overline{I}_0}{\lambda_n J_0^2(\lambda_n) \sin(\overline{\upsilon}_n l)} \sin(\overline{\upsilon}_n \overline{z}) + \frac{\overline{I}_0 \cos(\overline{\upsilon}_n \overline{z})}{\lambda_n J_0^2(\lambda_n)} \right] J_1(\lambda_n \overline{r}) \right.$$

$$\left. + \sum_{n=k+1}^{\infty} \left[\frac{\overline{I}_l - \cosh(\overline{\upsilon}_n^* l) \overline{I}_0}{\lambda_n J_0^2(\lambda_n) \sinh(\overline{\upsilon}_n^* l)} \sinh(\overline{\upsilon}_n^* \overline{z}) + \frac{\overline{I}_0 \cosh(\overline{\upsilon}_n^* \overline{z})}{\lambda_n J_0^2(\lambda_n)} \right] J_1(\lambda_n \overline{r}) \right\}^2 + \frac{\overline{D}}{\overline{r}^2} \Bigg)^{\frac{1}{2}} - \frac{\sqrt{\overline{D}}}{\overline{r}} e^{-\frac{K}{4} \mathrm{Re} \overline{r}^2}$$

Vita

Georges Henri Akiki was born in Jounieh on May 21st, 1986 to Henri and Hoda Akiki from Zouk Mikael, Kesrouan, Lebanon. After finishing at Antonine Sisters School, Ghazir, in 2004, he began his undergraduate studies at Notre Dame University, Louaize, where he graduated in February of 2009 as the Valedictorian of the Faculty of Engineering. He received the Dean's Award for Academic Excellence and a Bachelor of Engineering degree with Highest Distinction (Summa Cum Laude) in Mechanical Engineering.

Georges joined the University of Tennessee Space Institute in Fall 2009 where he is presently studying the subject of Fluid Mechanics under the direction of Dr. Majdalani, with special emphasis on swirl-dominated flows. In 2009, he received the J. B. Dicks Scholarship and, in April 2011, his paper with Dr. Majdalani won the first place award in the Masters Division at the 62nd Southeastern Regional Student Conference of the American Institute of Aeronautics and Astronautics. Georges will be graduating with a Master of Science degree in Aerospace Engineering from the University of Tennessee (UTSI) in August of 2011. He is a member of ASME, AIAA, and the Order of the Engineer.